

# Quantum quench spectroscopy of a Luttinger liquid: Ultrarelativistic density wave dynamics due to fractionalization in an XXZ chain

Matthew S. Foster,<sup>1,\*</sup> Timothy C. Berkelbach,<sup>2,†</sup> David R. Reichman,<sup>2</sup> and Emil A. Yuzbashyan<sup>1</sup>

<sup>1</sup>*Center for Materials Theory, Department of Physics and Astronomy,  
Rutgers University, Piscataway, NJ 08854, USA*

<sup>2</sup>*Department of Chemistry, Columbia University, New York, New York 10027, USA*

(Dated: November 7, 2018)

We compute the dynamics of localized excitations produced by a quantum quench in the spin 1/2 XXZ chain. Using numerics combining the density matrix renormalization group and exact time evolution, as well as analytical arguments, we show that fractionalization due to interactions in the pre-quench state gives rise to “ultrarelativistic” density waves that travel at the maximum band velocity. The system is initially prepared in the ground state of the chain within the gapless XY phase, which admits a Luttinger liquid (LL) description at low energies and long wavelengths. The Hamiltonian is then suddenly quenched to a band insulator, after which the chain evolves unitarily. Through the gapped dispersion of the insulator spectrum, the post-quench dynamics serve as a “velocity microscope,” revealing initial state particle correlations via space time density propagation. We show that the ultrarelativistic wave production is tied to the particular way in which fractionalization evades Pauli-blocking in the zero-temperature initial LL state.

PACS numbers: 71.10.Pm, 05.45.Yv, 64.60.Ht, 67.85.-d

## I. INTRODUCTION

In the labyrinth of one-dimensional (1D) quantum many-body physics, the Luttinger liquid (LL) lurks around nearly every corner. It emerges as the low energy field theory description of interacting Bose gases, gapless quantum spin chains, fermion lattice models (Hubbard, etc.), electrons in metallic carbon nanotubes, and chiral quantum Hall edge states.<sup>1–3</sup> Luttinger liquid physics is universal: it reduces the complexities of myriad microscopic models to the hydrodynamics of free bosons.

Despite its apparent simplicity, the LL description of interacting fermions exhibits a number of rather peculiar properties, due to the advent of quasiparticle *fractionalization*. The elementary excitations of a LL are collective density waves that carry fractional (electric or number) charge, relative to the “bare” fermionic constituents; injecting a bare fermion into a LL causes it to “break up” into many pieces. This collectivization of the dynamics due to fractionalization leads to a host of predicted anomalies, including the low bias suppression of the tunneling density of states, and perfect insulating behavior at zero temperature due to the presence of even a single impurity.<sup>4</sup> For spinful fermions, fractionalization induces spin-charge separation.<sup>2,5</sup> Interestingly enough, zero temperature dc transport in a clean quantum wire through ideal Fermi liquid leads shows no signature of fractionalization; the conductance is quantized to  $e^2/h$  per channel, irrespective of the interactions.<sup>6</sup>

In this paper, we describe a “transport” effect that directly exhibits fractionalization in a LL, observed in the dynamics of a density fluctuation following a sudden quantum quench. In a quantum quench, a system is prepared in an eigenstate of some initial Hamiltonian. In our case, we take the ground state of an XXZ chain with a non-uniform density profile, which possesses a low-

energy LL description. At the time of the quench, by external means a sudden deformation is affected upon the Hamiltonian, which subsequently drives the unitary

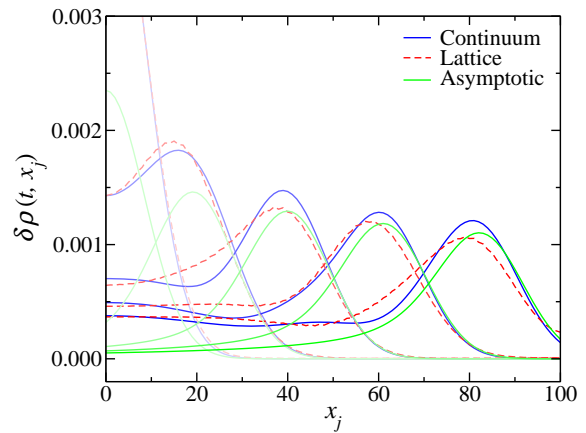


FIG. 1. Ultrarelativistic wave generated from an initial density bump, following an interacting quench. The Luttinger liquid ground state of an interacting XXZ chain is time-evolved according to a non-interacting, band insulator Hamiltonian. The density  $\delta\rho(t, x_j)$  due to the inhomogeneity is plotted at time slices  $t = 0, 12, 24, 36,$  and  $48$  after the quench; fainter (bolder) traces depict earlier (later) times. The evolution is symmetric about  $x_j = 0$ . In this figure, red dashed lines were obtained from a combination of DMRG and exact time evolution for the XXZ chain, while blue solid lines are the prediction of continuum sine-Gordon field theory. The curves marked “asymptotic” are the analytical result for the “regularized supersoliton,” obtained in Eq. (3.48). The initial coupling strength is  $\gamma = -0.872$ , corresponding to  $\sigma = 0.7$ . The initial bump has width  $\Delta = 12$  and weight  $Q = 0.10$ ; the mass gap is  $M = 1/8$ . The continuum data obtains from numerical integration of Eq. (3.47) with  $\alpha = 0.75$  and  $\zeta = 1$ .

post-quench dynamics. Here, the post-quench spectrum consists of non-interacting fermions, with a Hamiltonian that possesses a gapped, band insulator ground state (the XX chain in the presence of a sublattice staggered external field). We show that the relative fractionalization of the pre-quench system (due to interparticle interactions) leads to the production of “ultrarelativistic” density waves after the quench. These waves travel at the maximum band velocity, and exhibit a particular shape set by the interaction strength. The propagating density waves are “elementary excitations” of the post-quench non-equilibrium state; they occur because the fractionalized density inhomogeneity of the initial LL “injects” high momentum excitations into the post-quench band insulator. By contrast, under the same conditions a quench from the ground state of the non-interacting Fermi gas (the XX point of the XXZ chain) into the band insulator yields only dispersive density dynamics, a consequence of Pauli-blocking. Our setup can be viewed as a “quench spectroscopy” of fractionalization in a Luttinger liquid.

In the last decade, rapid experimental progress<sup>7</sup> in ultracold atoms and optical lattice gases has transported far-from-equilibrium many body physics fully into the quantum realm. In these systems, the quantum quench has emerged as a primary tool with which to investigate dynamics. Quenches have been performed in boson<sup>8–11</sup> and fermion<sup>12–14</sup> systems, with and without optical lattices, in one, two, and three dimensions. An ultracold gas can be very well isolated from its environment, and provides an unprecedented degree of control in terms of realizing model systems and manipulating their parameters.<sup>7</sup> Theoretical work has focused primarily on thermalization,<sup>15–21</sup> quantum critical scaling and defect production,<sup>22–26</sup> and correlation functions in spatially homogeneous systems.<sup>27–36</sup> Prior art on Luttinger liquid, sine-Gordon, and XXZ chain quenches includes that of Refs. 17, 19, 21, 29–34, 37–39. Wavepackets have been previously employed in the study of excitations induced by a *local* quench,<sup>40–42</sup> in which the Hamiltonian deformation is restricted to a spatial subregion of the larger system. The characterization of spatially inhomogeneous dynamics following a *global* parameter quench (as studied here) is a more recent development.<sup>37–39,43,44</sup>

Many of the previous schemes proposed or executed in the theoretical<sup>15,16,20,45,46</sup> and experimental<sup>8,9,13,14</sup> literature can be termed “hard quenches.” In these works, large changes in a parameter value or trap geometry lead to the excitation of novel high energy states<sup>8,9,16,45</sup> whose physics has little to do with the low-energy sectors of *either* the initial or final Hamiltonians (for an interesting exception, see Ref. 47). Our goal in this paper is different: we use a “soft quench” (defined below) as a low-energy probe of the initial state.

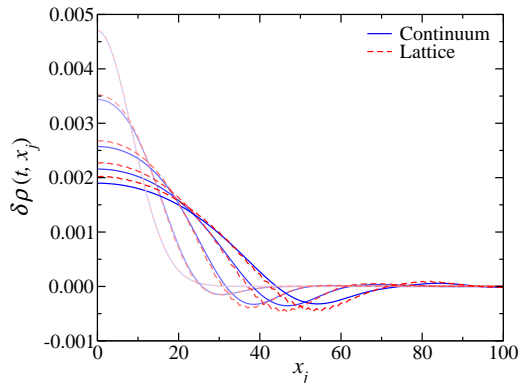


FIG. 2. Dispersive decay of a density bump following a non-interacting ( $\gamma = \sigma = 0$ ), non-relativistic ( $M\Delta = 3/2$ ) quench. This is the same as Fig. 1, but for a quench from a non-interacting Fermi gas to a band insulator. Parameters  $\Delta$ ,  $Q$ , and  $M$  are as in Fig. 1. Red dashed lines are the results of exact diagonalization of the lattice Hamiltonian, while blue solid lines are the continuum predictions.

## A. Overview

### 1. XXZ quench protocol; velocity microscope

We study the dynamics following a quantum quench in the 1D spin 1/2 XXZ chain. Working in the equivalent spinless (or spin-polarized) fermion representation, we investigate the time evolution of the particle density induced by a non-uniform initial state. Other works treating XXZ and sine-Gordon quenches subject to initial state inhomogeneity include Refs. 37–39; see Sec. V C for a discussion.

We consider a system initially prepared in the ground state of the XXZ chain in its gapless XY phase, subject to an external field. The field induces a localized “bump” in the density profile of the otherwise spatially homogeneous system. This state is further characterized by the spin anisotropy  $\gamma$  of the pre-quench  $\hat{S}_i^z \hat{S}_{i+1}^z$  coupling, i.e. the four fermion interaction strength. The gapless XY phase of the XXZ chain admits a low energy Luttinger liquid (LL) description.<sup>1,2</sup> At time  $t = 0$ , the system Hamiltonian is deformed discontinuously:  $\gamma$  is set to zero, while a sublattice-staggered external field is simultaneously applied along the length of the chain, opening up a gap in the spectrum. In the fermion language, the ground state of the post-quench (“final”) Hamiltonian is a non-interacting band insulator with a doubled unit cell.

The lattice quench with  $\gamma = 0$  in the initial XY state is special, because both the initial and final Hamiltonians are non-interacting in the fermion language. We dub this the “non-interacting” quench; the exact solution can be written for the time evolution of the density expectation value. By contrast, for  $\gamma \neq 0$  (“interacting” quench) the initial Hamiltonian is interacting in the fermion language and not soluble by elementary means. Although the XXZ chain is integrable, the non-uniform density profile makes

difficult the application of the Bethe ansatz method. Instead, in this paper we use the Density Matrix Renormalization Group (DMRG) to numerically compute correlation functions of the initial ground state. For both the non-interacting and interacting quenches, the dynamics generated by the non-interacting band insulator Hamiltonian are determined exactly. This allows us to avoid the use of more computationally intensive, time-dependent DMRG calculations. We exploit this advantage to analyze larger system sizes than previous numerical quench studies of the XXZ chain.<sup>17,34</sup>

The idea behind this setup is to use the quench into a gapped, dispersive phase as a “velocity microscope” on the initial correlated LL state. The non-uniform initial density profile creates additional excitations *on top of* the homogeneous bath induced by the global parameter quench, leading to real space dynamics that can in principle be directly observed. Particles composing space time density fluctuations are excited with a broad range of momenta; these are velocity-resolved by the dispersive post-quench spectrum. By contrast, time evolution with a generic gapless post-quench Hamiltonian in 1D (such as that governing a continuum conformal field theory) produces only pure left- and right-moving “ultrarelativistic” waves, regardless of the structure of the initial state.<sup>28,29</sup>

Throughout this work we make the crucial assumption of a “soft quench,” defined as follows. The magnitude of the gap in the post-quench Hamiltonian is specified by a dimensionless parameter  $Ma$ , where  $1/M$  gives the “Compton wavelength” for the low energy, massive excitations of the band insulator, and  $a$  denotes the lattice spacing. In addition, we assume a Gaussian density inhomogeneity in the initial state of width  $\Delta$ . The assumption of a “soft” quench requires that

$$a \ll \frac{1}{M} \lesssim \Delta, \quad (1.1)$$

i.e. that the low-energy Compton wavelength dwarfs the lattice spacing, while the width of the initial state inhomogeneity exceeds the Compton wavelength. The first assumption guarantees that the gap opens in the low-energy sector of the band Hamiltonian. The second  $M\Delta \gtrsim 1$  assures that any excitation of large-momentum particles post-quench arises from the correlated character of the LL, and not the excessive “squeezing” of the initial density bump.

Despite the requirement in Eq. (1.1), we will consider quenches with “intermediate” to “large” values of the initial XXZ interaction strength  $\gamma$ , approaching the ferromagnetic transition at  $\gamma = -1$ . It is far from obvious that a change from  $|\gamma| \lesssim 1$  to  $\gamma = 0$  preserves the notion of a “soft quench” as articulated above. Because the low-energy description throughout the gapless phase is a LL, it is nevertheless the case.

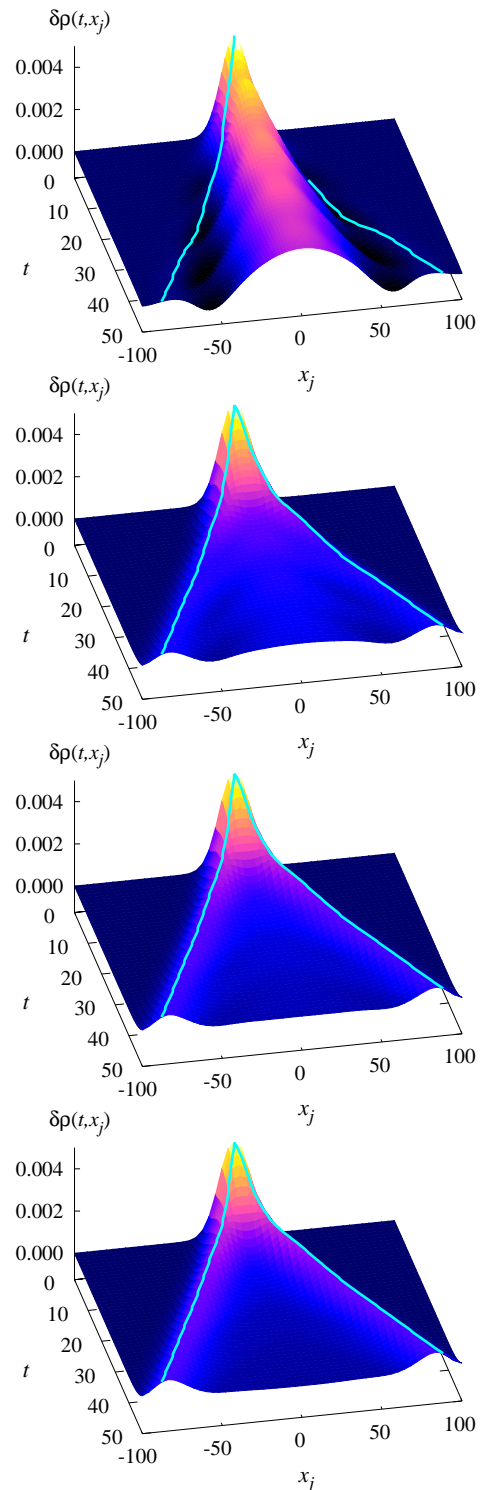


FIG. 3. Post-quench evolution of a density bump: dependence on initial state interparticle interaction strength. Each subpanel exhibits a three-dimensional view of a lattice quench (obtained by DMRG + exact time evolution) into the gapped band insulator;  $Q$ ,  $\Delta$ , and  $M$  are the same as in Figs. 1 and 2. The four frames depict quenches with increasing initial state interactions,  $\sigma = 0$  (non-interacting), 0.4, 0.7, and 1.0 (top to bottom). The cyan line demarks the maximum band propagation velocity (“speed of light”),  $v_{\max}(M = 1/8) \approx 1.77$ .

## 2. Sine-Gordon and “Supersolitons”

The XXZ quench can be interpreted as a lattice version of the continuum sine-Gordon field theory analyzed previously in Ref. 43. In that work, spatiotemporal dynamics were computed in a quench across a quantum critical point. In Ref. 43, a LL ground state subject to an inhomogeneous density modulation was time-evolved according to a translationally invariant, post-quench Hamiltonian favoring a gapped Mott ground state. The Mott Hamiltonian generating the dynamics was chosen to reside at the Luther-Emery<sup>48</sup> point of the sine-Gordon model, where the excitation spectrum consists entirely of non-interacting, massive Dirac fermions.<sup>1,2,49</sup> In the XXZ chain quench studied here, the final state band insulator carriers play the role of the non-interacting Dirac fermions that compose the sine-Gordon spectrum at the Luther-Emery point; the Mott gap of the sine-Gordon model is here substituted by the band gap.

A localized density inhomogeneity in the sine-Gordon quench launches ultrarelativistic, non-dispersing traveling waves, dubbed “supersolitons” in Ref. 43. The supersoliton exhibits a rigid shape, propagates at the “speed of light”  $v_F$  (the Fermi velocity), and possesses an amplitude that grows in time as  $t^{\sigma/2}$ . The exponent  $\sigma \geq 0$  characterizes the fractionalization of the initial LL state relative to the final Mott insulator. For the case  $\sigma = 0$  (non-interacting quench), there is no fractionalization and no supersoliton; the density dynamics of such a quench with  $M\Delta \gtrsim 1$  show only dispersive broadening.

In this work, we demonstrate that the supersoliton arises in the sine-Gordon quench for  $\sigma > 0$  due to the particular way in which LL fractionalization evades Pauli-blocking. This is made explicit through a calculation of the local phase space (Wigner) distribution in the pre-quench LL. The result is a power-law occupation of momentum states in the post-quench insulator that translates into a singular peak at  $v_F$  in the corresponding (local) velocity distribution. Because velocity is conserved by the post-quench Hamiltonian, the spectral weight associated to the singularity is translated at  $v_F$ . By contrast, a non-interacting quench with  $\sigma = 0$  and  $M\Delta \gg 1$  excites only small velocities  $v \lesssim v_F/M\Delta$ .

A key point is that it is the long-distance behavior of correlations in the initial state that permits the evasion of Pauli-blocking in the fractionalized case. Although lattice details can and do modify the ultraviolet behavior of correlations in the XXZ chain considered here, the fundamental distinction between non-interacting and interacting quenches remains a robust feature of the soft quench satisfying Eq. (1.1).

## 3. Preview of numerical results

We defer a detailed discussion of our XXZ chain quench results to the main text; the impatient reader may consult Sec. V for a summary. Instead, we exhibit a

few graphs that demonstrate the qualitative difference between the interacting and non-interacting quenches. Fig. 1 shows the “ultrarelativistic” density wave launched in an interacting quench satisfying the constraint in Eq. (1.1). (We set the lattice spacing  $a = 1$ ). By contrast, Fig. 2 depicts a non-interacting quench; in this case, only dispersive broadening of the initial density inhomogeneity is seen. The parameters in these two figures are the same, except for the interaction strength, quantified by a parameter  $\sigma(\gamma)$ . For a non-interacting quench one has  $\sigma(\gamma = 0) = 0$ ; otherwise  $\sigma > 0$  and increases monotonically with  $|\gamma|$ . The evolution of an XXZ chain quench as a function of the interaction strength  $\sigma$  is depicted as a 3D plot sequence in Fig. 3.

The blue continuous curves in Figs. 1 and 2 are obtained using an ultraviolet-regularized version of the sine-Gordon quench studied in Ref. 43. The regularization models the effects of neglected lattice scale details in a very crude way. The regularization cuts off the amplification of the supersoliton predicted for the pure sine-Gordon quench; it also leads to a modification of its interaction-dependent shape. Because of the close agreement between the field theory and lattice results, we interpret the ultrarelativistic density wave appearing in the interacting quench (Figs. 1 and 3) as a “regularized” supersoliton.

We emphasize that the quench dynamics described in this paper are fully quantum coherent; the absence of interparticle scattering in the post-quench band insulator prevents dephasing or thermalization. The “fractionalized” density dynamics reflect the many-body entanglement of the initial gapless state. Future work incorporating integrability-preserving interactions post-quench could prove particularly interesting, as discussed in the Conclusion.

## B. Outline

The organization of this paper is as follows. In Sec. II, we define the pre- and post-quench XXZ Hamiltonians and set up the dynamics to be computed. In Sec. III, we provide a comprehensive analysis linking the XXZ chain quench studied here to the corresponding version in the continuum, low-energy sine-Gordon field theory. We begin in Sec. III A with a quick review of single particle relativistic wavepacket mechanics, where we emphasize the distinction between “relativistic” and “non-relativistic” wavepacket propagation. In Sec. III B, we describe the solution to the pure sine-Gordon quench. We identify the supersoliton, discussed previously in Ref. 43. The global and local (Wigner) distributions induced in the lattice and continuum quenches are discussed in Sec. III C, wherein the origin of the supersoliton is revealed. In Sec. III D, the ultraviolet modifications of the sine-Gordon theory necessary to model the lattice quench are articulated, and relevant time scales are defined.

Numerical results obtained for the time evolution of

the XXZ chain quench are presented and discussed in Sec. IV. Results for the non-interacting and interacting quenches are exhibited and compared to the regularized sine-Gordon theory. We summarize our conclusions in Sec. V, and finish with a discussion of open questions. The asymptotic analysis method used to obtain key analytical results is explicated in Appendix A. Appendix B recapitulates the notion of fractionalization in a Luttinger liquid. In Appendix C, we derive the local (Wigner) velocity distributions induced by the initial state inhomogeneity, in the interacting and non-interacting continuum quenches.

## II. QUENCH SETUP

### A. Lattice model

In a (sudden) quantum quench, one prepares the system in an eigenstate of an initial Hamiltonian  $H^{(i)}$ , and subsequently time evolves under a different final Hamiltonian,  $H^{(f)}$ . We consider the XXZ spin 1/2 Heisenberg chain,

$$H = -2J \sum_i \left( \hat{S}_i^x \hat{S}_{i+1}^x + \hat{S}_i^y \hat{S}_{i+1}^y - \gamma \hat{S}_i^z \hat{S}_{i+1}^z \right) - \sum_i \mu_i \hat{S}_i^z. \quad (2.1)$$

Via the Jordan-Wigner transformation, the spin chain is equivalent to a model of spinless (or spin-polarized) fermions whose Hamiltonian is given by

$$H = -J \sum_i c_i^\dagger c_{i+1} + \text{H.c.} + 2J\gamma \sum_i \delta n_i \delta n_{i+1} - \sum_i \mu_i \delta n_i, \quad (2.2)$$

where  $J$  denotes the nearest-neighbor hopping amplitude,  $2J\gamma$  is a nearest-neighbor density-density interaction strength, and  $\mu_i$  represents a site-dependent chemical potential. In Eq. (2.2),  $c_i$  and  $c_j^\dagger$  satisfy  $c_i c_j^\dagger + c_j^\dagger c_i = \delta_{ij}$ , and  $\delta n_i \equiv c_i^\dagger c_i - 1/2$ . We will quench from a ground state in the gapless XY phase of this Hamiltonian (labeled by the dimensionless interaction strength  $\gamma$ ) to a non-interacting, band insulator state. The latter is induced via the application of a unit cell doubling, sublattice-staggered chemical potential. Furthermore, by applying a localized Gaussian chemical potential, we will induce a density inhomogeneity into the initial state whose dynamics will reveal the effects of our quantum quench.

The zero temperature phase diagram for the XXZ chain in Eq. (2.2) with  $\mu_i = \mu$  (const.) is sketched in Fig. 4. At zero chemical potential, the chain is in its gapless, power-law correlated XY phase for  $-1 < \gamma \leq 1$ . For  $\gamma > 1$  ( $\gamma < -1$ ), the spin chain assumes long-range Ising antiferromagnetic (ferromagnetic) order and the spectrum gaps out. We note that the thickness of the chemical potential window over which power-law XY

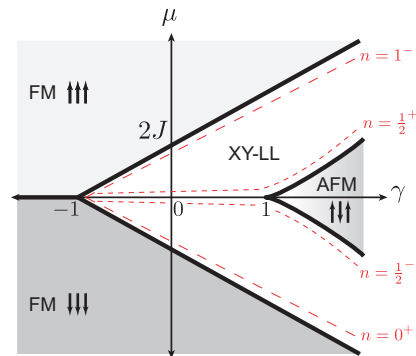


FIG. 4.  $T = 0$  ground state phase diagram for the XXZ chain.<sup>50</sup> Red dashed lines correspond to constant fermion density contours.

order occurs (at fermion densities between 0 and 1 per site) narrows to zero upon approaching the ferromagnetic transition at  $\gamma = -1$ .

For the quantum quench studied here, the initial and final lattice Hamiltonians are given by

$$H^{(i)} = -J \left[ \sum_i c_i^\dagger c_{i+1} + \text{H.c.} - 2\gamma \sum_i \delta n_i \delta n_{i+1} \right] - \sum_i \mu_i^{(0)} \delta n_i, \quad (2.3a)$$

$$H^{(f)} = -J \left[ \sum_i c_i^\dagger c_{i+1} + \text{H.c.} - 2Ma \sum_i (-1)^i \delta n_i \right]. \quad (2.3b)$$

We assume periodic boundary conditions in a chain of  $N = L/a$  sites, with  $a$  the lattice spacing, so that  $c_{N+1} = c_1$ . We always take  $N$  to be an even integer. The initial Hamiltonian  $H^{(i)}$  is tuned to reside in its gapless XY phase, so that  $-1 < \gamma \leq 1$ .

In Eq. (2.3a) above,

$$\mu_i^{(0)} = \frac{Q\sqrt{\pi}}{\Delta} \frac{u(\gamma)}{K(\gamma)} e^{-x_i^2/\Delta^2} \quad (2.4)$$

is the localized chemical potential used to introduce a particle density inhomogeneity near the center of the chain; we have introduced the spatial coordinate  $x_i = (i - N/2)a$  such that  $x_{N/2} = 0$  and  $x_{N/2+1} = a$  straddle the chain center. The parameters  $Q$  and  $\Delta$  set the “strength” and width of the Gaussian potential, respectively. Two additional parameters that enter into Eq. (2.4) are the sound velocity  $u$  and the Luttinger parameter  $K$ . These coefficients completely determine the character of the low-energy field theory description of the XXZ chain in its critical XY phase, in equilibrium. In the absence of an external chemical potential,  $u$  and  $K$  can

be obtained from the Bethe ansatz, yielding<sup>1</sup>

$$u(\gamma) = Ja \frac{\pi \sqrt{1-\gamma^2}}{\arccos(\gamma)}, \quad (2.5a)$$

$$K(\gamma) = \frac{\pi}{2[\pi - \arccos(\gamma)]}, \quad (2.5b)$$

such that  $u(0) = 2Ja \equiv v_F$  and  $K(0) = 1$ . Here,  $v_F$  denotes the band Fermi velocity at half-filling with  $M = 0$ . We have included the ratio  $u/K$  in the definition of the local potential so as to keep the initial induced density inhomogeneity approximately constant with varying interaction strength  $\gamma$ .

The spectrum of  $H^{(f)}$  [Eq. (2.3b)] is

$$E_k = \pm 2J \sqrt{\cos^2(ka) + (Ma)^2}. \quad (2.6)$$

The staggered potential, which doubles the unit cell, introduces a bandgap in the spectrum at  $k_F = \pi/2a$  with magnitude  $E_g = 4JMa$ .

Based on the analysis of the continuum sine-Gordon quench in Ref. 43, we expect the post-quench system response to be governed by the dynamical exponent,

$$\begin{aligned} \sigma(\gamma) &\equiv \frac{1}{2} \left[ K(\gamma) + \frac{1}{K(\gamma)} \right] - 1 \\ &= \frac{2[\arcsin(\gamma)]^2}{\pi^2 + 2\pi \arcsin(\gamma)}. \end{aligned} \quad (2.7)$$

Such an interaction-dependent exponent characterizes the (critical) power-law behavior exhibited by correlation functions in gapless 1D quantum systems that possess a low-energy LL description. At  $\gamma = 0$  (non-interacting quench),  $\sigma$  assumes its minimum value of zero. At  $\gamma = 1$ , on the precipice of the instability to Ising antiferromagnetism,  $\sigma = 1/4$ . By contrast,  $\sigma$  diverges upon approaching  $\gamma = -1$  from above.

In what follows, we set  $J = 1$  and  $a = 1$ , thereby measuring energies in units of the transfer integral  $J$  and distances in units of the lattice spacing  $a$ . Our observable of interest will be the time-evolved density at each site of the lattice, i.e.

$$\rho(t, x_i) \equiv \langle \delta n_i(t) \rangle = \langle 0 | e^{iH^{(f)}t} c_i^\dagger c_i e^{-iH^{(f)}t} | 0 \rangle - 1/2, \quad (2.8)$$

where  $|0\rangle$  is the ground state of the initial Hamiltonian  $H^{(i)}$ .

## B. Dynamics; non-interacting quench

For both the interacting ( $\gamma \neq 0$ ) and non-interacting ( $\gamma = 0$ ) quenches, the dynamics are obtained by solving the Heisenberg equation of motion for the annihilation operator  $c_i(t)$  at site  $i$  using  $H^{(f)}$  [Eq. (2.3b)]. The result

is

$$\begin{aligned} c_i(t) &= \sum_{j=1}^N c_j(0) \left\{ G^{(1)}(t, i-j) \right. \\ &\quad + [(-1)^i + (-1)^j] G^{(2)}(t, i-j) \\ &\quad \left. + (-1)^{i+j} G^{(3)}(t, i-j) \right\} \\ &\equiv \sum_{j=1}^N \mathcal{G}_{ij}(t) c_j(0), \end{aligned} \quad (2.9)$$

where  $c_j(0)$  denotes the Schrödinger picture operator, and

$$G^{(a)}(t, j) = \frac{1}{N} \sum_{n_k=1}^{N/2} \exp\left(i \frac{2\pi n_k j}{N}\right) \tilde{G}^{(a)}\left(t, \frac{2\pi n_k}{N}\right), \quad (2.10)$$

with

$$\tilde{G}^{(1)}(t, k) = \cos(E_k t) - i \frac{\epsilon_k}{E_k} \sin(E_k t), \quad (2.11a)$$

$$\tilde{G}^{(2)}(t, k) = -i \frac{2M}{E_k} \sin(E_k t), \quad (2.11b)$$

$$\tilde{G}^{(3)}(t, k) = \cos(E_k t) + i \frac{\epsilon_k}{E_k} \sin(E_k t). \quad (2.11c)$$

In Eq. (2.11),  $\epsilon_k = -2 \cos(k)$  and  $E_k$  was defined by Eq. (2.6). The post-quench dynamics of the number density are subsequently given by

$$\rho(t, x_i) = \sum_{j, j'=1}^N [\mathcal{G}_{ij}^*(t) \mathcal{G}_{ij'}(t) \mathcal{C}(x_j, x_{j'})], \quad (2.12)$$

where all information about the initial state is encoded in the static correlation function (single-particle density matrix)

$$\mathcal{C}(x_j, x_{j'}) \equiv \langle 0 | c_j^\dagger(0) c_{j'}(0) | 0 \rangle; \quad (2.13)$$

$|0\rangle$  denotes the ground state of  $H^{(i)}$ .

For the special case of the non-interacting quench,  $\mathcal{C}(x_j, x_{j'})$  is obtained by diagonalizing an  $N \times N$  matrix. We denote the single particle Hamiltonian implied in Eq. (2.3a) with  $\gamma = 0$  by  $\hat{h}$ . In this case, the correlator is given by

$$\mathcal{C}(x_j, x_{j'}) = \left[ \hat{U} \hat{P}(-\hat{h}_D) \hat{U}^\dagger \right]_{j, j'}, \quad (2.14)$$

where  $\hat{U}^\dagger \hat{h} \hat{U} = \hat{h}_D$  diagonalizes the single particle Hamiltonian, and  $\hat{P}(-\hat{h}_D)$  projects onto the (filled) negative energy states of the diagonalized  $\hat{h}_D$ . Combining Eqs. (2.14) and (2.12) gives the formal solution to the non-interacting quench. In practice, because of the inhomogeneity, we compute the single-particle matrix in Eq. (2.14) numerically.

### III. CONTINUUM VS. LATTICE

#### A. Warm-up: Relativistic wavepacket dynamics of a single massive Dirac particle

Before turning to the continuum sine-Gordon quench, we pause to consider a toy problem: the time evolution of a Gaussian wavepacket for a single, massive Dirac fermion in 1D. This material is standard, but we include it to emphasize several important points regarding disparate regimes of relativistic wave propagation, and to clarify the similarities and differences between single particle wave packet mechanics and the many particle quantum quench problem studied in this paper.

The post-quench, band insulator Hamiltonian in Eq. (2.3b) exhibits a gap  $E_g = 2v_F M$ , centered at  $k = k_F = \pi/2$ . Linearizing and truncating the band structure to modes near  $k_F$ , one obtains

$$\bar{H}^{(f)} = \int dx \psi^\dagger \hat{h} \psi, \quad (3.1)$$

where the single particle Hamiltonian is given by

$$\hat{h} = v_F \left[ -i\hat{\sigma}^3 \frac{d}{dx} + M\hat{\sigma}^2 \right], \quad (3.2)$$

and the 2-component Dirac spinor  $\psi(x)$  has the Fourier transform

$$\psi(k) \equiv \begin{bmatrix} \psi_1(k) \\ \psi_2(k) \end{bmatrix} = \begin{bmatrix} e^{-i\pi/4} c(k + k_F) \\ e^{i\pi/4} c(k - k_F) \end{bmatrix}, \quad (3.3)$$

with  $0 \leq |k| \leq \Lambda \ll k_F$  ( $\Lambda$  is a momentum cutoff). The components  $\psi_1$  and  $\psi_2$  denote right- and left-movers in the massless limit. In Eq. (3.2), we have introduced a set of Pauli matrices  $\{\hat{\sigma}^{1,2,3}\}$  acting in the pseudospin space of  $\psi$ .<sup>51</sup> The Fermi velocity  $v_F = 2$ ; below we absorb it into the primed time,

$$t' \equiv v_F t. \quad (3.4)$$

In this section we take the system size  $L \rightarrow \infty$ .

We assume a Gaussian initial wavefunction for a particle in its rest frame,

$$\Psi_0(x) = \frac{1}{(\pi\Delta^2)^{1/4}} e^{-x^2/2\Delta^2} \begin{bmatrix} \Psi_{0,1} \\ \Psi_{0,2} \end{bmatrix}, \quad (3.5)$$

with  $|\Psi_{0,1}|^2 = |\Psi_{0,2}|^2 = 1/2$ . In this equation and the ones that follow,  $\Psi$  denotes a single particle wavefunction; its time evolution is determined by  $\hat{h}$  in Eq. (3.2) via the Schrödinger equation. It is useful to write the solution at times  $t \geq 0$  in two different ways. One way is

$$\Psi(t, x) \equiv \Psi_+(t, x) + \Psi_-(t, x), \quad (3.6)$$

where the components  $\Psi_{\mu=\pm}(t, x)$  are defined via

$$\begin{aligned} \Psi_\mu(t, x) = & \frac{\sqrt{\Delta} M}{(4\pi)^{3/4}} \int_{-\infty}^{\infty} dz e^{-(\frac{M\Delta}{2})^2 [\cosh(2z)-1]} \\ & \times e^{-i\mu A(t', x) \cosh[z - \mu z_0(t', x)]} \\ & \times (\Psi_{0,1} - \mu i e^{-\mu z} \Psi_{0,2}) \begin{bmatrix} e^{\mu z} \\ \mu i \end{bmatrix}. \end{aligned} \quad (3.7)$$

An alternative representation for  $\Psi(t, x)$  is given by

$$\begin{aligned} \Psi(t, x) = & \frac{1}{(\pi\Delta^2)^{1/4}} \left\{ \begin{bmatrix} \Psi_{0,1} e^{-(x-t')^2/2\Delta^2} \\ \Psi_{0,2} e^{-(x+t')^2/2\Delta^2} \end{bmatrix} \right. \\ & \left. + \int_{-t}^t dy e^{-\frac{(x-y)^2}{2\Delta^2}} \begin{bmatrix} \bar{G}^{(1)}(t', y) & \bar{G}^{(2)}(t', y) \\ -\bar{G}^{(2)}(t', y) & \bar{G}^{(3)}(t', y) \end{bmatrix} \begin{bmatrix} \Psi_{0,1} \\ \Psi_{0,2} \end{bmatrix} \right\}, \end{aligned} \quad (3.8)$$

where

$$\bar{G}^{(1)}(t, y) = -\frac{M}{2} \left[ \frac{t+y}{\sqrt{t^2-y^2}} \right] J_1[A(t, y)], \quad (3.9a)$$

$$\bar{G}^{(2)}(t, y) = -\frac{M}{2} J_0[A(t, y)], \quad (3.9b)$$

$$\bar{G}^{(3)}(t, y) = -\frac{M}{2} \left[ \frac{t-y}{\sqrt{t^2-y^2}} \right] J_1[A(t, y)], \quad (3.9c)$$

denote the  $M$ -dependent components of the Green's functions [from the continuum limit of Eq. (2.11)]. In Eq. (3.7),  $\tanh(z_0) = x/t'$ , while  $A(t', y) = M\sqrt{t'^2 - y^2}$ . Eqs. (3.6) and (3.7) follow from the momentum eigenstate expansion for the time evolution operator, while Eq. (3.8) obtains from the real space propagation amplitude. In Eq. (3.9), the symbols  $J_{\{0,1\}}$  denote Bessel functions of the first kind.

A basic consequence of relativistic quantum field theory is that a single particle cannot be confined to a region smaller than its Compton wavelength  $1/M$ . Localization to smaller scales induces particle energies in excess of the mass gap; in a many-particle theory, this typically leads to pair production out of the vacuum.

In single particle relativistic wave mechanics, one instead finds qualitatively different behavior for initial confinements  $\Delta \gg 1/M$  ("non-relativistic") and  $\Delta \ll 1/M$  ("relativistic"). We consider first the non-relativistic case. For  $M\Delta \gg 1$ , the argument of the exponential in Eq. (3.7) can be expanded to quadratic order in  $z$ . In

this approximation, one obtains

$$|\Psi(t, x)|^2 = \frac{1}{4\sqrt{\pi}\Delta\delta(t')} e^{-x^2/\Delta^2\delta^2(t')} \times \left\{ \begin{array}{l} 2 - \frac{2}{\delta(t')} \cos[2Mt' - \phi_0(t', x)] \\ + \frac{2t'}{M\Delta^2\delta(t')} \sin[2Mt' - \phi_0(t', x)] \\ + e^{1/[M\Delta\delta(t')]^2 + 2t'x/M^2\Delta^4\delta^2(t')} \\ \times \left[ \begin{array}{l} 1 + \frac{1}{\delta(t')} \cos[2Mt' - \phi_+(t', x)] \\ - \frac{t'}{M\Delta^2\delta(t')} \sin[2Mt' - \phi_+(t', x)] \end{array} \right] \\ + e^{1/[M\Delta\delta(t')]^2 - 2t'x/M^2\Delta^4\delta^2(t')} \\ \times \left[ \begin{array}{l} 1 + \frac{1}{\delta(t')} \cos[2Mt' - \phi_-(t', x)] \\ - \frac{t'}{M\Delta^2\delta(t')} \sin[2Mt' - \phi_-(t', x)] \end{array} \right] \end{array} \right\}, \quad (3.10)$$

where the scale factor  $\delta(t) = \sqrt{1 + t^2/M^2\Delta^4}$ ,  $\phi_{\{0,+,-\}}(t, x)$  denote some phase factors.<sup>52</sup> For the initial spinor components in Eq. (3.5), we have made the choice  $\Psi_{0,\{1,2\}} = \exp(\mp i\pi/4)/\sqrt{2}$ , so that  $\Psi_0(x)$  is invariant under time-reversal and parity operations.<sup>53</sup>

To the lowest order in  $1/M\Delta$ , Eq. (3.10) reduces to the usual non-relativistic formula

$$|\Psi(t, x)|^2 = \frac{1}{\sqrt{\pi}\Delta\delta(t')} e^{-x^2/\Delta^2\delta^2(t')}.$$

At smaller values of  $1/M\Delta$ , the oscillatory character of Eq. (3.10) becomes important, and one observes the “Zitterbewegung” phenomenon: the evolving probability density exhibits an undulatory envelope that beats at the “interband” frequency  $\omega = 1/2M$ . These oscillations occur because the eigenstate synthesis of the initial Gaussian [Eq. (3.5)] requires larger contributions from negative energy states as the width  $\Delta$  is narrowed.

In the ultrarelativistic limit  $M = 0$ , Eq. (3.8) implies that

$$|\Psi(t, x)|^2 = \frac{1}{2\sqrt{\pi}\Delta} \left[ e^{-(x-t')^2/\Delta^2} + e^{-(x+t')^2/\Delta^2} \right].$$

By contrast, when  $0 < M\Delta \ll 1$ , the propagation is relativistic but dispersive. In the long time limit, the second term on the right-hand side of Eq. (3.8) is dominated by the diagonal Green’s functions. Close to the right light-cone edge  $|x - t| \lesssim \Delta$ , for  $t' \gg t'_{\text{disp}}$  one obtains

$$\Psi(t, x) \sim \frac{1}{(\pi\Delta^2)^{1/4}} e^{-(x-t')^2/2\Delta^2} f\left(\frac{t'}{t'_{\text{disp}}}, \frac{x-t'}{\Delta}\right) \begin{bmatrix} \Psi_{0,1} \\ 0 \end{bmatrix} + \text{dispersive background}, \quad (3.11)$$

where

$$t'_{\text{disp}} = 1/2M^2\Delta.$$

The function

$$f(\alpha, \beta) = \int_0^\infty dw \left[ 1 - e^{-\beta w^2/\alpha - w^4/2\alpha^2} \right] J_1(w)$$

vanishes in the limit  $\alpha \rightarrow \infty$ .

In the XXZ chain quantum quench studied in this paper, it will prove essential to distinguish relativistic vs. non-relativistic initial conditions using the width  $\Delta$  of the Gaussian chemical potential inhomogeneity in Eq. (2.4) and the bandgap parameter  $M$  in the post-quench Hamiltonian  $H_f$  [Eq. (2.3b)]. Examples of single particle non-relativistic and relativistic propagation are shown in Fig. 5.

### B. Sine-Gordon quench and “supersolitons”

We now consider the continuum limit of the XXZ quench defined by  $H^{(i)}$  and  $H^{(f)}$  [Eqs. (2.3a) and (2.3b)]. This problem was previously analyzed in Ref. 43. In this section, we provide the solution to the sine-Gordon quench and a brief recapitulation of the results found in Ref. 43. In Sec. IIID, we consider the modification of these results due to the presence of irrelevant operators

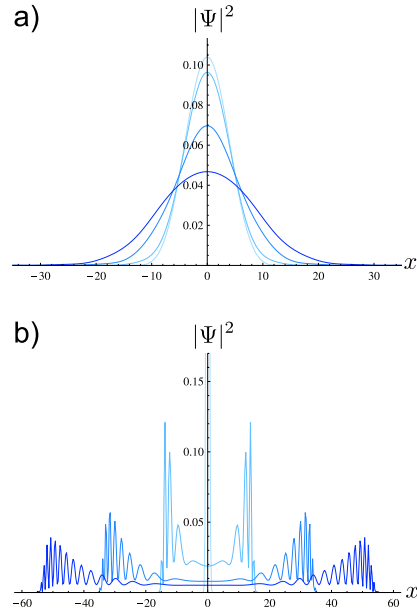


FIG. 5. Examples of single particle, massive Dirac equation wave packet propagation, obtained via numerical integration of Eqs. (3.6) and (3.7). The case (a) corresponds to a “non-relativistic” initial condition, the Gaussian in Eq. (3.5) with  $\Delta = 5/M$ . The “relativistic” case is illustrated in (b), with an initial  $\Delta = 0.5/M$ . Here  $M \equiv 1$ , and data is shown at times  $t = 0, 15, 35$ , and  $55$ ; fainter (bolder) traces depict earlier (later) times.



(i.e., lattice-scale details left out of the renormalizable continuum field theory).

The massive Dirac continuum limit for the final state Hamiltonian  $\bar{H}^{(f)}$  was derived in the last section, Eqs. (3.1)–(3.3). Since this Hamiltonian is non-interacting, we can construct a formal solution to the quench dynamics by solving the Heisenberg equations of motion for the Dirac spinor  $\psi(t, x)$  [c.f. Eq. (2.9)]. The result is

$$\psi(t, x) = \int_{-t'}^{t'} dy \hat{\mathcal{J}}(t', y) \psi(0, x - y), \quad (3.12a)$$

where

$$\hat{\mathcal{J}}(t, y) \equiv \hat{\mathcal{J}}_0(t, y) + \hat{\mathcal{J}}_M(t, y), \quad (3.12b)$$

$$\hat{\mathcal{J}}_0(t, y) = \begin{bmatrix} \delta(y - t) & 0 \\ 0 & \delta(y + t) \end{bmatrix}, \quad (3.12c)$$

$$\hat{\mathcal{J}}_M(t, y) = \begin{bmatrix} \bar{G}^{(1)}(t, y) & \bar{G}^{(2)}(t, y) \\ -\bar{G}^{(2)}(t, y) & \bar{G}^{(3)}(t, y) \end{bmatrix}. \quad (3.12d)$$

Eq. (3.12) is identical to the propagation amplitude transcribed in the last section [Eq. (3.8)], after replacing the single particle wave function  $\Psi_0(x)$  with the Schrödinger picture field operator  $\psi(0, x)$ . In these equations,  $t' = v_F t$  [Eq. (3.4)], while the Green's functions  $\bar{G}^{(1,2,3)}(t, y)$  were defined by Eq. (3.9).

The post-quench fermion density is given by

$$\rho(t, x) = \int_{-t'}^{t'} dy_1 \int_{-t'}^{t'} dy_2 \left[ \hat{\mathcal{J}}^\dagger(t', y_1) \hat{\mathcal{J}}(t', y_2) \right]_r^s \times \mathcal{C}_s^r(x - y_1, x - y_2), \quad (3.13)$$

where all information about the initial state is encoded in the correlation function

$$\mathcal{C}_s^r(x_1, x_2) \equiv \langle \bar{0} | \psi^{r\dagger}(0, x_1) \psi_s(0, x_2) | \bar{0} \rangle. \quad (3.14)$$

In Eqs. (3.13) and (3.14), the indices  $r, s \in \{1, 2\}$ ; repeated indices are summed.

The pre-quench system is described by the ket  $|\bar{0}\rangle$ , which is taken as the ground state of the Luttinger liquid Hamiltonian

$$\bar{H}^{(i)} = \int dx \left[ -v_F \psi^\dagger \left( i \hat{\sigma}^3 \frac{d}{dx} \right) \psi - \mu^{(0)}(x) : \psi^\dagger \psi : + 2\gamma v_F : \psi^\dagger \psi \psi^\dagger \psi : \right]. \quad (3.15)$$

Eq. (3.15) gives the continuum limit of  $H^{(i)}$  in Eq. (2.3a), after discarding all irrelevant operators; here,  $\mu^{(0)}(x)$  represents the long wavelength, continuum approximation to the lattice potential  $\mu_i^{(0)}$ .<sup>54</sup> The symbol  $:\dots:$  denotes normal-ordering.

Using abelian bosonization rules,<sup>1,2,5</sup> we rewrite Eq. (3.15) as

$$\bar{H}^{(i)} = \int dx \left[ \frac{uK}{2} \left( \frac{d\phi}{dx} \right)^2 + \frac{u}{2K} \left( \frac{d\theta}{dx} \right)^2 - \frac{\mu^{(0)}(x)}{\sqrt{\pi}} \frac{d\theta}{dx} \right]. \quad (3.16)$$

In our conventions, the fermion current components are bosonized as

$$\{J^0, J^1\} \equiv \{\psi^\dagger \psi, \psi^\dagger \hat{\sigma}^3 \psi\} = \left\{ \frac{1}{\sqrt{\pi}} \frac{d\theta}{dx}, \frac{1}{\sqrt{\pi}} \frac{d\phi}{dx} \right\}, \quad (3.17)$$

and satisfy  $[J^0(x), J^1(x')] = -(i/\pi)(d/dx)\delta(x - x')$ . The sound velocity  $u$  and the Luttinger parameter  $K$  in Eq. (3.16) are given by

$$u = \frac{v_F}{K}, \quad K = \frac{1}{\sqrt{1 + \frac{4\gamma}{\pi}}}. \quad (3.18)$$

With  $v_F = 2$ , these agree with the Bethe ansatz results in Eq. (2.5) only to the first order in  $\gamma$ .

When expressed in terms of the boson variables, the post-quench massive Dirac Hamiltonian in Eq. (3.1) becomes the sine-Gordon model

$$\bar{H}^{(f)} = v_F \int dx \left[ \frac{1}{2} \left( \frac{d\phi}{dx} \right)^2 + \frac{1}{2} \left( \frac{d\theta}{dx} \right)^2 + \frac{M}{\pi\alpha} \cos(\sqrt{4\pi}\theta) \right]. \quad (3.19)$$

The variable  $\alpha$  appearing in the prefactor of the cosine term carries units of length, and is formally introduced by the bosonization procedure.<sup>1,5</sup>

While  $\bar{H}^{(i)}$  [Eq. (3.16)] assumes a non-interacting form when expressed in boson variables,  $\bar{H}^{(f)}$  becomes the non-linear sine-Gordon theory. By contrast,  $\bar{H}^{(f)}$  [Eq. (3.1)] is non-interacting in terms of the Fermi field  $\psi$ , while  $\bar{H}^{(i)}$  [Eq. (3.15)] incorporates four fermion interactions. For a quench with  $\gamma \neq 0$ , there is no common language in which both  $\bar{H}^{(i)}$  and  $\bar{H}^{(f)}$  can be simultaneously expressed as non-interacting Hamiltonians. We refer to this generic scenario as the “interacting” quench in the sine-Gordon theory. We reserve the appellation “non-interacting” for the exceptional case with  $\gamma = 0$ , where both  $\bar{H}^{(i)}$  and  $\bar{H}^{(f)}$  are bilinear in fermions. The post-quench dynamics exhibited for each case are different, as discussed below.

Expressing the fermions in Eq. (3.14) as vertex operators in the bosonic language,<sup>1</sup> the initial state correlation function components evaluate to

$$\mathcal{C}_1^1(x_1, x_2) = \frac{ic_N \alpha^\sigma}{2\pi} \exp \left[ i \frac{K}{u} \int_{x_1}^{x_2} dy \mu^{(0)}(y) \right] \times \frac{\text{sgn}(x_1 - x_2)}{|x_1 - x_2|^{\sigma+1}}, \quad (3.20a)$$

$$\mathcal{C}_2^2(x_1, x_2) = \frac{-ic_N \alpha^\sigma}{2\pi} \exp \left[ -i \frac{K}{u} \int_{x_1}^{x_2} dy \mu^{(0)}(y) \right] \times \frac{\text{sgn}(x_1 - x_2)}{|x_1 - x_2|^{\sigma+1}}, \quad (3.20b)$$

$$\mathcal{C}_2^1(x_1, x_2) = \mathcal{C}_1^2(x_1, x_2) = 0 \quad (L \rightarrow \infty). \quad (3.20c)$$

In these equations, the external chemical potential manifests in a gauge “string” due to the axial anomaly.<sup>2,55</sup>

The coefficient  $\alpha$  was introduced in Eq. (3.19); the parameter  $c_N$  is a numerical normalization constant.<sup>56</sup> The off-diagonal components of  $\mathcal{C}_s^r(x_1, x_2)$  ( $r \neq s$ ) vanish in the thermodynamic limit  $L \rightarrow \infty$ .

The essential character of the initial Luttinger liquid state is encoded in the dynamic exponent  $\sigma$ , defined as

$$\sigma \equiv \frac{1}{2} \left( \frac{1}{K} + K \right) - 1. \quad (3.21)$$

For the non-interacting quench,  $K = 1$  and  $\gamma = \sigma = 0$ . By contrast, any  $K \neq 1$  ( $\gamma \neq 0$ ) gives  $\sigma > 0$ .<sup>57</sup> Eq. (3.20) implies that  $\sigma$  is twice the anomalous scaling dimension of  $\psi$  in the initial LL ground state.

Using Eq. (3.20), the integrals appearing in the final expression for the post-quench density expectation in Eq. (3.13) are ultraviolet convergent for  $0 \leq \sigma < 1$ . Over this range of initial conditions, we obtain a cutoff-independent prediction for the post-quench evolution of the number density in the continuum sine Gordon field theory. Similar expressions with identical convergence properties may be obtained for the kinetic and potential energy densities due to the inhomogeneous initial state chemical potential.<sup>43</sup>

The general characteristics of the long-time density dynamics implied by Eq. (3.13) and (3.20) for a generic initial state  $\mu^{(0)}(x)$  were discussed in Ref. 43. In this paper, we restrict our attention to the waves induced by a localized, Gaussian initial inhomogeneity,

$$\frac{K}{\mu} \mu^{(0)}(x) = \frac{Q\sqrt{\pi}}{\Delta} e^{-x^2/\Delta^2}. \quad (3.22)$$

Combining Eqs. (3.22), (3.20), and (3.13) gives an exact integral expression for the post-quench density expectation evolution after the sine-Gordon quench. In the long time limit  $t \gg 1/v_F M$ , the requisite integrals yield to a systematic asymptotic analysis, as explained in Appendix A. One thereby obtains the exact leading asymptotic behavior

$$\begin{aligned} \rho(t, x) = & \frac{Q}{2\sqrt{\pi}\Delta} e^{-(x-t')^2/\Delta^2} \\ & - \frac{Q}{2\Delta} \frac{\Gamma(1-\sigma)}{\Gamma(\frac{1+\sigma}{2})} \left[ \frac{(M\alpha)^2 t'}{\sqrt{2}\Delta} \right]^{\sigma/2} F_\sigma \left( \frac{x-t'}{\Delta} \right) \\ & + \{x \rightarrow -x\}, \end{aligned} \quad (3.23)$$

where

$$F_\sigma(z) \equiv \exp(-z^2/2) D_{\sigma/2}(\sqrt{2}z), \quad (3.24)$$

and  $D_\nu(x)$  denotes the parabolic cylinder function. In Eq. (3.23), we have used the explicit expression for the normalization constant  $c_N$ .<sup>56</sup> Regardless, for  $\sigma > 0$  (interacting quench) the prefactor of the second term in Eq. (3.23) is in some sense arbitrary, due to the  $\alpha$  factor. This ambiguity can be resolved if a conventional normalization is adopted for the vertex function correlators in

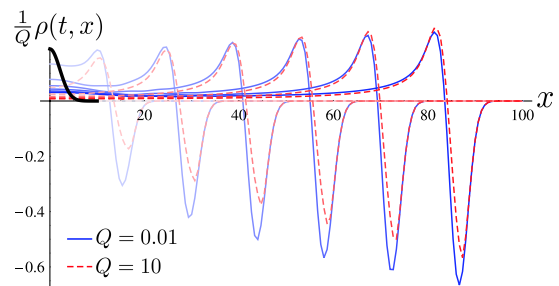


FIG. 6. The right-moving “supersoliton” obtained in the interacting sine-Gordon quench. The number density evolution after a Luttinger liquid to insulator quench is depicted for a Gaussian initial density profile (heavy black line), with  $\sigma = 0.7$ ,  $\Delta = 3$ , and  $M = 15/16$ , obtained via numerical integration of the exact bosonization result [Eqs. (3.13) and (3.20), using Eq. (3.22)]. Time series for two different  $Q$  are plotted; the densities are normalized relative to these. The evolution is reflection symmetric about  $x = 0$ .

Eq. (3.20).<sup>58</sup> The derivation of Eq. (3.23) is sketched in Appendix A.

For the interacting quench with  $0 < \sigma < 1$ , Eq. (3.23) describes the propagation of right and left moving “supersolitons” launched from the Gaussian initial condition, in the long time limit. A right-moving supersoliton is depicted in Fig. 6. From the equation, it is evident that the supersoliton does not disperse. In the long-time limit, the response to the initial chemical potential (and thus the initial state density inhomogeneity) is linear, regardless of the strength of  $Q$  in Eq. (3.22). The supersoliton features an amplitude that grows in time as power law, with growth exponent  $\sigma/2$ ; subleading terms neglected in Eq. (3.23) decay for  $\sigma > 0$ . The peculiar shape of the supersoliton implied by Eq. (3.24) obtains because the quench kernel effectively takes a fractional derivative  $(d/dx)^{\sigma/2}$  of the input profile.<sup>43</sup> The total number fluctuation induced by the inhomogeneity is conserved by the supersoliton, since the second term in Eq. (3.23) integrates to zero over  $x \in \mathbb{R}$ .<sup>59</sup> Finally, we note that Eq. (3.23) holds for generic  $M\Delta$ : the supersoliton arises for both “relativistic” ( $M\Delta \gg 1$ ) and “non-relativistic” ( $M\Delta \ll 1$ ) initial density profiles (c.f. Sec. III A).

By contrast, the non-interacting quench with  $\sigma = 0$  exhibits no amplification. For  $M\Delta \gg 1$  (“non-relativistic” initial condition), one finds simple dispersive broadening, qualitatively similar to the single particle wavepacket spreading in Fig. 5(a). Examples of non-interacting quenches with non-relativistic initial conditions are shown in Fig. 7. For the non-interacting quench, the response is given entirely by terms neglected as subleading (for  $\sigma > 0$ ) in Eq. (3.23); indeed, the right-hand side of this expression vanishes for  $\sigma = 0$ .

Non-interacting quenches with “relativistic” ( $M\Delta \ll 1$ ) initial conditions exhibit a different behavior, qualitatively similar to the single particle wavepacket evolution depicted in Fig. 5(b): the initial Gaussian density bump blows apart into left and right-moving wave trains, with

leading edges that rip along lightcone. In this sense, the non-interacting quench with  $M\Delta \ll 1$  behaves similar to the supersoliton, which also propagates relativistically. At short timescales  $t \lesssim 1/v_F M$ , the interacting and non-interacting quenches in fact exhibit qualitatively similar dynamics for relativistic initial conditions. However, the non-interacting quench evolution shows no amplification in the long time limit, and the generated wave train exhibits no static, non-dispersing structure. In the numerical results for the XXZ chain quench presented in Sec. IV, we will restrict our attention to non-relativistic initial conditions, in order to avoid possibly confusing the supersoliton with the trivial (and essentially single particle) effect of squeezing the initial density wavepacket to a width narrower than the Compton wavelength.

Finally, we note that setting  $M = 0$  in Eq. (3.23) gives the result appropriate to a Luttinger liquid to Luttinger liquid quench—the initial density disturbance is merely propagated along the light cone without dispersion, as expected for dynamics generated by a critical state. This case was previously considered in Ref. 38.

The physics of the interacting and non-interacting quenches are fundamentally distinguished by the advent of quasiparticle *fractionalization* in the interacting case. The interacting nature of the pre-quench initial ground state  $|\bar{0}\rangle$  relative to the post-quench Hamiltonian  $\bar{H}^{(f)}$  is implied by Eq. (3.15) with  $\gamma \neq 0$ , which expresses  $\bar{H}^{(i)}$  in terms of the “final state” fermion  $\psi$ . The presence of interparticle interactions in  $\bar{H}^{(i)}$  means the fermion  $\psi$  is not a “natural” propagating degree of freedom in the initial state Luttinger liquid.<sup>60</sup> Equivalently, the “quasiparticles” of the LL carry a fraction  $\sqrt{K}$  of the  $\psi$  fermion number charge; we say that the initial LL state is *fractionalized* with respect to the final band insulating state. This notion is made explicit in Appendix B. Fractionalization due to the presence of interparticle interactions is a ubiquitous feature in 1D, responsible e.g. for spin-charge separation in quantum wires.<sup>1,2</sup>

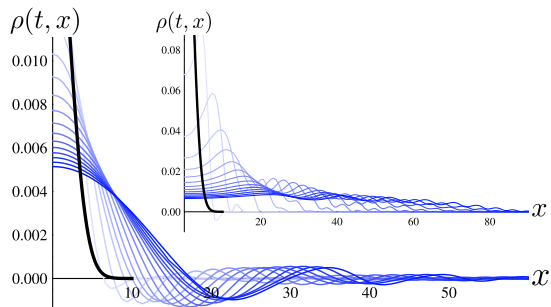


FIG. 7. The number density evolution as in Fig. 6, but for the non-interacting quench  $K = 1$  ( $\sigma = 0$ ). The initial bump (heavy black line) has area  $Q = 0.1$  in the main figure and  $Q = 1$  in the inset; in both cases  $\Delta = 3$  and  $M = 15/16$ . The evolution is reflection symmetric about  $x = 0$ . Now there is no fractionalization of the initial LL quasiparticles with respect to the insulator and, consequently, the dynamics are simply dispersive with no supersolitons or inhomogeneity growth.

We interpret the supersoliton and the amplification effect that arises in the sine-Gordon quench for the interacting case as a *spectroscopy* of the initial LL state.<sup>43</sup> The key ingredients are quasiparticle fractionalization of the initial state relative to the excitation spectrum of the post-quench Hamiltonian, and fact that the post-quench Hamiltonian is gapped. In the next section and in Appendix C, we show that fractionalization leads to an anomalous momentum dependence in the Wigner distribution function of the excited post-quench quasiparticles, due to the inhomogeneity. The low-energy dispersion of the gapped final state characterized by  $M$  translates this into a divergent velocity distribution, giving rise to the supersoliton. By contrast, for a non-relativistic density profile with  $M\Delta \gg 1$ , Pauli-blocking suppresses the excitation of large velocities in the non-interacting quench. The distinction arises due to the long-distance behavior of correlations in the initial state, and is not destroyed by lattice effects. At the same time, we will see in Sec. III D that the advent of the lattice does modify the post-quench dynamics, but in way that can be parametrically controlled by the system size.

### C. Quasiparticle distribution functions: continuum and lattice quenches

We consider the post-quench distribution of *final state* quasiparticles, in the sine-Gordon and lattice quenches. Time evolution is generated by the final state Hamiltonian, which is translationally invariant and non-interacting in terms of band fermions for both the lattice [ $H^{(f)}$ , Eq. (2.3b)] and continuum [ $\bar{H}^{(f)}$ , Eq. (3.1)] theories. The global momentum distribution of excited quasiparticles induced by the quench in each case constitutes a static quantity, which does not encode information about the density inhomogeneity. The physics of the supersoliton resides in the local Wigner function, which is discussed subsequently.

#### 1. Global distribution function

We consider first the continuum sine-Gordon quench. The final state Hamiltonian  $\bar{H}^{(f)}$  in Eq. (3.1) and (3.2) can be rewritten as

$$\bar{H}^{(f)} = \int \frac{dk}{2\pi} \varepsilon_k \left[ a_k^\dagger a_k + b_k^\dagger b_k \right], \quad (3.25)$$

where  $a_k$  ( $b_k$ ) annihilates a particle (hole) with momentum  $k$ , and

$$\varepsilon_k = v_F \sqrt{k^2 + M^2}. \quad (3.26)$$

The particle and hole operators are related to  $\psi$  via

$$\begin{aligned} \begin{bmatrix} \psi_1(k) \\ \psi_2(k) \end{bmatrix} &= \frac{a_k}{\sqrt{1+s^2(k)}} \begin{bmatrix} 1 \\ is(k) \end{bmatrix} \\ &+ \frac{b_{-k}^\dagger}{\sqrt{1+s^2(-k)}} \begin{bmatrix} 1 \\ -is(-k) \end{bmatrix}, \end{aligned} \quad (3.27)$$

where

$$s(k) \equiv \frac{\varepsilon_k - v_F k}{v_F M}.$$

We define the occupation numbers

$$\begin{aligned} n_+(k) &\equiv \langle \bar{0} | a_k^\dagger a_k | \bar{0} \rangle, \\ n_-(k) &\equiv \langle \bar{0} | b_k^\dagger b_k | \bar{0} \rangle, \end{aligned} \quad (3.28)$$

in which  $|\bar{0}\rangle$  denotes the ground state of the pre-quench Hamiltonian  $\bar{H}^{(i)}$ , Eqs. (3.15) and (3.16).

For the translationally invariant case  $\mu^{(0)}(x) = 0$ , one can show that

$$n_+(k) = n_-(k) = \frac{1}{2} + \frac{k}{\varepsilon_k} \mathcal{F}(k), \quad (3.29)$$

where

$$\mathcal{F}(k) = \langle \bar{0} | \psi_1^\dagger(k) \psi_1(k) | \bar{0} \rangle - \frac{1}{2} \quad (3.30)$$

and  $\mathcal{F}(-k) = -\mathcal{F}(k)$ . The form of Eqs. (3.29) and (3.30) follows from Eq. (3.27) and the imposition of the sum rule (canonical anticommutation relations) upon correlators of the fermion components  $\psi_i(k)$ .

In the case of the non-interacting quench ( $\sigma = 0$ ), one finds  $\mathcal{F}(k) = -(1/2) \text{sgn}(k)$ , so that

$$n_\pm(k) = \frac{1}{2} \left( 1 - \frac{|k|}{\sqrt{k^2 + M^2}} \right). \quad (3.31)$$

This occupancy factor peaks to a value of one-half at  $k = 0$ , and decays as  $M^2/k^2$  for  $|k| \gg M$ . The density of particles or holes excited by the quench is thus ultraviolet finite and equal to  $M/2\pi$ . The associated kinetic energy density is given by the difference of the pre- and post-quench Hamiltonian zero point energy densities, and is logarithmically divergent.

The calculation for the interacting case is more subtle, due to an ultraviolet divergence. We must compute

$$\langle \bar{0} | \psi_1^\dagger(k) \psi_1(k) | \bar{0} \rangle = \frac{c_N \alpha^\sigma}{2\pi} \int_{-\infty}^{\infty} dx \frac{e^{ikx} (\alpha + ix)}{(\alpha^2 + x^2)^{1+\sigma/2}}, \quad (3.32)$$

which is the Fourier transform of the initial state correlator in Eq. (3.20a) with  $\mu^{(0)} = 0$ , retaining the soft cutoff  $\alpha$ .<sup>1</sup> The prefactor  $c_N$  appears explicitly in Ref. 56. Performing an expansion in  $k\alpha$  and extracting  $\mathcal{F}(k)$ , we finally obtain

$$\begin{aligned} n_\pm(k) &= \frac{1}{2} \left[ 1 - \frac{|k|}{\sqrt{k^2 + M^2}} \frac{\Gamma(\frac{1-\sigma}{2})}{\Gamma(\frac{1+\sigma}{2})} \left( \frac{|k|\alpha}{2} \right)^\sigma \right] \\ &+ \mathcal{O}(|k|\alpha), \end{aligned} \quad (3.33)$$

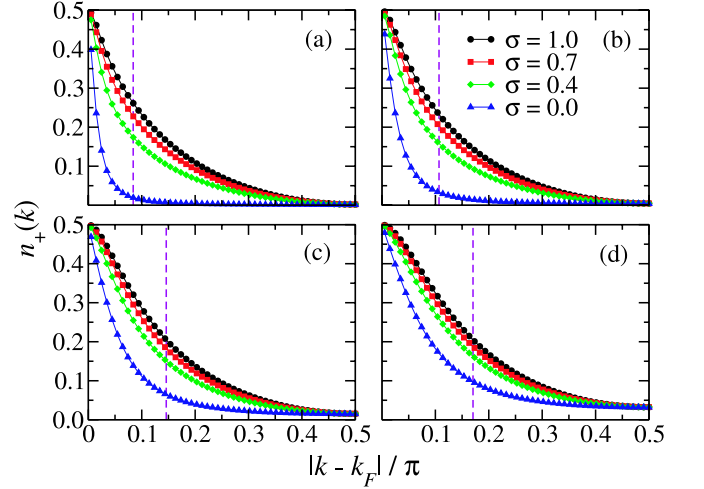


FIG. 8. Occupancy of momentum states in the upper (conduction) band after the lattice XXZ quench (obtained via DMRG), for the four values of the dynamical exponent  $\sigma$  given in the legend. The occupancies are plotted for four different choices of the band-gap parameter,  $M = 3/40$  (a),  $1/8$  (b),  $1/4$  (c), and  $3/8$  (d). In each subplot, the dashed vertical line marks the wavenumber  $k_{\max}(M)$  at which the final state Hamiltonian band group velocity is maximized,  $v(k_{\max}; M) = \max[dE_k/dk] \equiv v_{\max}(M)$ ; see Sec. IV B 2, Eqs. (4.3) and (4.4).

valid for  $0 \leq \sigma < 1$ . Eq. (3.33) holds only for  $|k|\alpha$  small, where the second term on the right-hand side trails the first. At such wavevectors,  $n_\pm$  is enhanced relative to the non-interacting case in Eq. (3.31), indicating that the interacting quench induces a stronger excitation of the post-quench quasiparticles. Clearly Eq. (3.33) becomes unphysical for sufficiently large  $|k|$ ; the global distribution function cannot be uniquely defined (i.e., its value will depend upon the regularization procedure) in the continuum, interacting sine-Gordon quench.

In Fig. 8, we exhibit  $n_+(k)$  for the lattice quench in a finite size system of 202 sites, obtained via numerical density matrix renormalization group calculations (see Sec. IV for details). The occupancy is defined as in Eq. (3.28), except that the continuum state  $|\bar{0}\rangle$  is replaced by  $|0\rangle$ , the ground state of  $H^{(i)}$  in Eq. (2.3a);  $a_k$  now denotes the lattice conduction band annihilation operator.

## 2. Wigner function, fractionalization, and the origin of the supersoliton

Eqs. (3.31) and (3.33) have been calculated for the case of the homogeneous quench. In the infinite system size limit, these equations also apply in the presence of an arbitrary initial state chemical potential  $\mu^{(0)}(x)$  that vanishes faster than  $1/x$  as  $|x| \rightarrow \infty$ . The effects of the inhomogeneous density profile in the initial state can be extracted from the “local” (Wigner) distribution

function.<sup>61</sup>

The main idea is conveyed by the ground state Wigner function for the right-moving fermion  $\psi_1(x) \equiv \mathcal{R}(x)$  in the inhomogeneous Luttinger liquid, defined as

$$\begin{aligned} n_{\mathcal{R}}(k; R) &\equiv \int dx_d e^{-ikx_d} \langle \bar{0} | \mathcal{R}^\dagger \left( R - \frac{x_d}{2} \right) \mathcal{R} \left( R + \frac{x_d}{2} \right) | \bar{0} \rangle \\ &= \int \frac{dq}{2\pi} e^{iqR} \langle \bar{0} | \tilde{\mathcal{R}}^\dagger \left( k - \frac{q}{2} \right) \tilde{\mathcal{R}} \left( k + \frac{q}{2} \right) | \bar{0} \rangle. \end{aligned} \quad (3.34)$$

Here  $|\bar{0}\rangle$  is the ground state of  $\bar{H}^{(i)}$  in Eq. (3.15), which has the density expectation  $\langle \bar{0} | \mathcal{R}^\dagger(x) \mathcal{R}(x) | \bar{0} \rangle = \rho_0(x)/2$ , where

$$\rho_0(x) \equiv \frac{K}{\pi u} \mu^{(0)}(x). \quad (3.35)$$

The global momentum distribution and the position space density expectation value can both be extracted from the Wigner function (Appendix C). Although we employ it here to gain intuition about the local momentum profile induced by  $\rho_0(x)$ , strictly speaking  $n_{\mathcal{R}}(k; R)$  cannot be interpreted as a probability distribution<sup>62</sup> (it can take negative values), because momentum and position are canonically conjugate quantum observables.

We let  $\delta n_{\mathcal{R}}(k; R)$  denote the linear response due to  $\rho_0(x)$ , after subtracting off the homogeneous (global) background. Using the correlation function in Eq. (3.20a), we find

$$\begin{aligned} \delta n_{\mathcal{R}}(k; R) &= c_N \alpha^\sigma \int \frac{dq}{2\pi} \frac{\tilde{\rho}_0(q)}{q} e^{iqR} \\ &\quad \times \left[ \begin{array}{l} \text{sgn} \left( k + \frac{q}{2} \right) \mathcal{G}_\sigma \left( \left| k + \frac{q}{2} \right|; \zeta \right) \\ - \text{sgn} \left( k - \frac{q}{2} \right) \mathcal{G}_\sigma \left( \left| k - \frac{q}{2} \right|; \zeta \right) \end{array} \right], \end{aligned} \quad (3.36)$$

where

$$\mathcal{G}_\sigma(|p|; \zeta) \equiv \int_0^\infty \frac{dy}{y} \frac{1}{(y^2 + \zeta^2)^{\sigma/2}} \sin(|p|y). \quad (3.37)$$

The parameter  $\zeta$  is an ultraviolet regularization length, introduced here for later use in the context of the lattice quench defined in Sec. II A (see Sec. III D). The pure continuum theory has  $\zeta = 0$ , for which Eq. (3.37) is convergent when  $0 \leq \sigma < 1$ .

For the special case of a non-interacting Fermi gas ( $\sigma = 0$ ),  $\mathcal{G}_0(|p|; \zeta) = \pi/2$ , independent of  $|p|$ , so that

$$\begin{aligned} \delta n_{\mathcal{R}}(k; R) &= \frac{\pi}{2} \int \frac{e^{iqR} dq}{2\pi} \frac{\tilde{\rho}_0(q)}{q} \\ &\quad \times \left[ \text{sgn} \left( k + \frac{q}{2} \right) - \text{sgn} \left( k - \frac{q}{2} \right) \right]. \end{aligned} \quad (3.38)$$

This expression vanishes for  $|q| < 2|k|$ , i.e. unless the creation and annihilation operators in Eq. (3.34) carry

momentum with opposite signs. This is a simple consequence of Pauli blocking. The result can be understood via perturbation theory: let  $|\bar{0}\rangle \equiv |\bar{0}\rangle_0 + |\delta\rangle$ ;  $|\bar{0}\rangle_0$  denotes the homogeneous vacuum, while  $|\delta\rangle$  gives the response to  $\rho_0(x)$ . To first order in  $|\delta\rangle$ , Eq. (3.34) vanishes unless the product  $\tilde{\mathcal{R}}^\dagger \left( k - \frac{q}{2} \right) \tilde{\mathcal{R}} \left( k + \frac{q}{2} \right)$  creates a particle-hole pair in  $|\bar{0}\rangle_0$  (acting to the left or to the right); Eq. (3.38) obtains from the overlap between this state and  $|\delta\rangle$ .

We consider a  $\rho_0(x)$  localized in position space, of characteristic width  $\Delta$ . For  $|k| \gg 1/\Delta$ , Eq. (3.38) implies that the  $k$ -dependence of the Wigner function is slaved to follow that of  $\tilde{\rho}_0(q)$ , with  $q \sim 2k$ . For a Gaussian inhomogeneity, this means a Gaussian fall off of the Wigner function in  $k$ . No matter how wide or narrow the initial packet is made, the large- $k$  asymptotic is always strongly suppressed.

By contrast, the situation for the interacting Luttinger liquid is quite different, Eq. (3.36) with  $\sigma > 0$ . Then, the kernel  $\mathcal{G}_\sigma(|p|; \zeta)$  depends upon  $|p|$ , and allows a contribution to  $\delta n_{\mathcal{R}}(k; R)$  from  $|q| < 2|k|$ , violating the Pauli blocking condition. For  $|k| \gg 1/\Delta$ , the dominant contribution comes from  $|q| \ll 2|k|$ , and the  $q$ -integration gives  $\delta n_{\mathcal{R}}(k; R) \propto \rho(R)$ . The  $k$ -dependence comes entirely from  $d\mathcal{G}_\sigma(|k|; \zeta)/d|k|$ , and is independent of the initial inhomogeneity profile: the  $R$ - and  $k$ -dependencies of the Wigner function *factorize*. For  $0 < \sigma < 1$  and  $\zeta = 0$ , the leading term in the  $|k| \gg 1/\Delta$  limit of Eq. (3.36) goes as

$$\delta n_{\mathcal{R}}(k; R) \sim c(\sigma) \alpha^\sigma |k|^{\sigma-1} \rho_0(R), \quad (3.39)$$

where the prefactor satisfies  $c(0) = 0$ .

In the sine-Gordon quench, the initial ‘‘momentum distribution’’ implied by Eq. (3.36) or (3.39) translates into a ‘‘velocity distribution’’ through the massive post-quench dispersion relation in Eq. (3.26); details are presented in Appendix C. In the non-interacting case, for a non-relativistic initial condition with  $M\Delta \gg 1$ , only small velocities  $v \lesssim v_F/M\Delta$  are excited [Eq. (C7) in Appendix C]. By contrast, an interacting quench with Eq. (3.39) induces a non-integrable divergence in the velocity distribution at the ‘‘speed of light’’  $v = v_F$  [Eq. (C8a)], signaling the presence of the non-dispersing supersoliton (recall that velocity is conserved by the post-quench Hamiltonian). Thus, the supersoliton arises due to the particular way in which quasiparticle fractionalization evades Pauli blocking in the initial LL ground state.

To gain further insight, consider a many-particle product state in a relativistic quantum theory, e.g.  $N$  particles are placed into  $N$  plane wave states with momenta  $\{k_i\}$ . In the thermodynamic limit  $N \rightarrow \infty$ , the system is described by a continuous distribution function  $n(k)$ , a well-defined (classical) observable for a product state. Suppose further that the corresponding velocity distribution  $n(v)$  exhibits a delta-function-like singularity at  $v = v_F$ . Then, a fraction of the density (determined by the weight of the singularity) at each point in space is translated at the speed of light. In particular, a fraction of any initial density inhomogeneity will propagate

at  $v = v_F$  without dispersion.

Even though this intuitive velocity distribution picture helps reveal the physical origin of the supersoliton, it is not entirely satisfactory. For example, a finite number of massive particles traveling at the speed of light implies an infinite kinetic energy. By contrast, although it propagates ultrarelativistically, the supersoliton carries finite total energy beyond that induced by the homogeneous quench.<sup>43</sup> The initial (inhomogeneous) Luttinger liquid is very far from a product state of the post-quench spectrum; indeed, the appearance of the exponent  $\sigma$  in Eqs. (3.33) and (3.39) indicates that quantum coherence (entanglement) plays a dominant role in the fractionalized density dynamics of the quench. Further, the Wigner function  $\delta n(k; R)$  is not really a phase space distribution function,<sup>62</sup> and the non-integrable velocity singularity in Eq. (C8a), Appendix C does not imply an extensive mass or energy flow. Instead, we interpret this divergence as signaling the supersoliton, an emergent, collective excitation of the post-quench non-equilibrium state that travels with velocity  $v_F$ .

Let us also note that the Wigner distribution post-quench is not a static object; the spatially-varying momentum profile in Eq. (3.39) implies that the shape of the density wave can evolve. In the unregularized sine-Gordon quench, this is the amplification effect exhibited in Fig. 6 and Eq. (3.23).

The ultraviolet effects induced by the presence of a lattice cannot alter the fundamental distinction between interacting and non-interacting quenches, because the long-distance behavior of  $\langle \bar{0} | \mathcal{R}^\dagger(0) \mathcal{R}(x) | \bar{0} \rangle$  determines the efficacy of Pauli blocking in Eq. (3.36) through Eq. (3.37). In the next section, we will nevertheless see that the modification of the short-distance structure of the theory [e.g.,  $\zeta > 0$  in Eq. (3.37)] does influence the post-quench dynamics.

Further details about the post-quench Wigner function can be found in Appendix C, where explicit formulae are given for the associated velocity distributions in the non-interacting and interacting quenches, incorporating the effects of ultraviolet regularization.

#### D. Irrelevant operators and UV regularization

So far, we have focused primarily on the Luttinger liquid to band insulator quench in the continuum sine-Gordon model. For a Gaussian initial density bump, the leading asymptotic result for the long-time limit [Eq. (3.23)] predicts the emergence of the supersoliton: a non-dispersive, relativistically-propagating density wave with an amplitude that grows as  $t^{\sigma/2}$ . This result applies to the integrable sine-Gordon field theory, in the absence of additional perturbations. We have considered only a particular case by assuming the non-interacting post-quench Hamiltonian in Eq. (3.1). This corresponds to the special Luther-Emery (LE) point in the sine-Gordon phase diagram.<sup>1,2,43</sup> Away from this point,  $\bar{H}^{(f)}$

would acquire a four-fermion interaction as in Eq. (3.15); bosonization links the sine-Gordon and massive Thirring models in the general case.<sup>55</sup> We postpone a discussion of the effects of interparticle collisions in the post-quench evolution until the end of Sec. V.

The sine-Gordon field theory arises as the low-energy description of many 1D solid state and cold atomic systems,<sup>1,3,63</sup> including the XXZ chain quench introduced in Sec. II A between  $H^{(i)}$  and  $H^{(f)}$  in Eq. (2.3). Details of the original “microscopic” formulation are expected to appear in the effective low-energy field theory as irrelevant operators.<sup>64</sup> Irrelevant operators typically exert a negligible effect upon low-energy, long-wavelength properties in a zero temperature field theory. Finiteness of correlation functions (up to logarithmic divergences subsumed by renormalization) and insensitivity to irrelevant operators go hand-in-hand.<sup>55,64</sup>

By contrast, the influence of irrelevant operators upon the strong non-equilibrium dynamics generated by a sudden quench remains largely unexplored territory. The incorporation of generic perturbations destroys some special properties that may be enjoyed by a given renormalizable theory, such as conformal invariance or, in the case of the 1D sine-Gordon model, integrability. On general grounds, a non-integrable many-body system prepared in an initial, non-thermal state is expected to thermalize (presumably due to quantum chaotic dynamics) in the long time limit.

In this paper, we do not mount a broad assault upon the important topics of integrability-breaking perturbations and thermalization. Even in equilibrium, the impact of irrelevant operators and integrability on correlation functions *at non-zero temperature* remains a contentious issue.<sup>42,65–73</sup> Here, we limit our focus to the post-quench wave train dynamics exemplified by the supersoliton. In particular, we would like to understand how irrelevant operators, or equivalently, lattice scale details and the presence of a finite ultraviolet cutoff, modify or suppress the supersoliton. Our considerations in this section will be used to interpret the numerical results for the XXZ chain quench presented in Sec. IV.

##### 1. Irrelevant operators: some examples

The XXZ chain quench introduced in Sec. II A takes the ground state  $|0\rangle$  of the XY phase Hamiltonian  $H^{(i)}$  in Eq. (2.3a), and evolves this state forward in time using the gapped band insulator Hamiltonian  $H^{(f)}$  defined via Eq. (2.3b). In the continuum field theory limit, lattice microscopics induce the addition of irrelevant operators to the sine-Gordon model Hamiltonians  $\bar{H}^{(i)}$  and  $\bar{H}^{(f)}$  [Eqs. (3.15), (3.16), and (3.1), (3.19)]. We now enumerate a few examples.

The *least* irrelevant operators  $\{\mathcal{O}_i(x)\}$  invariant under continuum versions of all lattice symmetries (time-reversal, parity, lattice translational invariance) carry the scaling dimension  $x_i = 4$  when added to the non-

interacting Dirac Hamiltonian in either Eq. (3.15) (with  $\gamma = 0$ ) or (3.1). We consider first the umklapp interaction operator<sup>5</sup>

$$\begin{aligned} \mathcal{O}_u(x) &\equiv 2 \left[ \left( \psi_1^\dagger \psi_2 \right)^2 + \left( \psi_2^\dagger \psi_1 \right)^2 \right] \\ &= -\frac{1}{(\pi\alpha)^2} \cos \left[ 2\sqrt{4\pi}\theta \right]. \end{aligned} \quad (3.40)$$

This operator appears as a lattice-induced modification (via  $H^{(i)}$ ) of the initial Luttinger liquid Hamiltonian  $\bar{H}^{(i)}$ , Eq. (3.15) or (3.16).<sup>5</sup> The dimension of the umklapp operator is  $x_1 = 4K$ , so that the associated coupling constant has dimension  $y_1 = 2(1 - 2K)$ , where  $K$  denotes the Bethe ansatz Luttinger parameter in Eq. (2.5b).<sup>64</sup> Thus the umklapp operator has  $y_1(K = 1) = -2$  at the free fermion point, while  $y_1(K = 1/2) = 0$  at the threshold of the Ising antiferromagnetic order [Eq. (2.5b) with  $\gamma \rightarrow 1$ ]. In our lattice quenches, we will focus upon  $\gamma < 0$ , so that  $K > 1$  and umklapps are strongly irrelevant.

As a second example, we consider the effect of band curvature (at half-filling), which gives the operator

$$\begin{aligned} \mathcal{O}_3(x) &\equiv -\psi^\dagger \left( i\hat{\sigma}^3 \frac{d^3}{dx^3} \right) \psi \\ &= -\frac{1}{4} \left[ \left( \frac{d^2\phi}{dx^2} \right)^2 + \left( \frac{d^2\theta}{dx^2} \right)^2 \right] \\ &\quad - \frac{\pi}{2^3} : \left[ \left( \frac{d\phi}{dx} + \frac{d\theta}{dx} \right)^4 + \left( \frac{d\phi}{dx} - \frac{d\theta}{dx} \right)^4 \right] : \end{aligned} \quad (3.41)$$

$\mathcal{O}_3$  arises as a modification of both  $\bar{H}^{(i)}$  and  $\bar{H}^{(f)}$ , due to the cosine dispersion of the lattice model.

We note that while the band curvature operator in Eq. (3.41) is bilinear in terms of fermions, both the umklapp and band curvature operators induce interparticle interactions in the boson language. This complication makes it difficult to determine the influence of either upon the interacting LL initial state  $|\bar{0}\rangle$ .

One can in principle treat non-bilinear irrelevant operators perturbatively, but several difficulties arise in attempting to account for their effects. First, the perturbation theory is badly ultraviolet divergent, and depends upon the way in which these divergences are regularized. A second, more serious (but intimately related) problem arises because the effects of irrelevant operators become strong at short distances. In the context of the quench, the goal is to construct the initial ground state correlator in Eq. (3.14), accounting for the effects of lattice scale details. These details should translate into a modification of the ideal Luttinger liquid correlation functions in Eq. (3.20) at short distances. However, the effects of irrelevant operators become strong in precisely this limit; the result is that perturbation theory breaks down, and a systematic accounting is only possible via an exact or approximate non-perturbative resummation.

Nevertheless, we show that a regularized version of the continuum sine-Gordon quench can be constructed which gives a reasonably good match to our finite system size numerics presented in Sec. IV. To motivate the regularization scheme that we employ, we consider the effect of a finite-ranged density-density interaction.<sup>1</sup> Instead of Eq. (3.16), one has the Hamiltonian

$$\begin{aligned} \bar{H}^{(i)} &= \frac{1}{2} \int dx \left[ \left( \frac{d\phi}{dx} \right)^2 + \left( \frac{d\theta}{dx} \right)^2 \right] \\ &\quad + \frac{1}{2\pi} \int dx dx' v(x-x') \frac{d\theta}{dx}(x) \frac{d\theta}{dx'}(x') \end{aligned} \quad (3.42)$$

where  $v(x) \equiv (2\gamma/\zeta) \exp(-|x|/\zeta)$  is a Yukawa-type potential that integrates to  $4\gamma$ , regardless of the range  $\zeta$ . The limit  $\zeta \rightarrow 0$  gives the purely local interaction implemented in Eq. (3.16).

Unlike the non-bilinear boson operators associated with umklapp and band curvature effects discussed above, the finite-range interaction in Eq. (3.42) can be treated non-perturbatively. The result is a modification of the Luttinger liquid correlator in Eq. (3.20); in the homogeneous limit with  $\mu^{(0)}(x) = 0$ , one obtains

$$\mathcal{C}_1^1(x, 0) = \frac{ic_N}{2\pi} \frac{\text{sgn}(x)}{|x|} \mathfrak{C}(x), \quad (3.43)$$

where

$$\begin{aligned} \mathfrak{C}(x) &= \exp \left\{ \int_0^\infty \frac{dq}{q} \sigma(q) [\cos(qx) - 1] \right\} \\ &\sim \left[ \frac{\zeta^2}{\zeta^2 + \beta x^2} \right]^{\sigma^{(0)}/2}. \end{aligned} \quad (3.44)$$

In this equation,

$$\sigma(q) \equiv \frac{1}{2} [K(q) + K^{-1}(q)] - 1, \quad (3.45a)$$

$$K(q) \equiv \left[ 1 + \frac{4\gamma}{\pi} \frac{1}{1 + (\zeta q)^2} \right]^{-1/2}. \quad (3.45b)$$

The variable  $\beta$  in Eq. (3.44) is some numerical constant. The effect of a finite interaction range  $\zeta > 0$  is to reduce the short-range scaling behavior ( $|x| \lesssim \zeta$ ) of the  $\psi$  fermion LL correlation functions in Eq. (3.20) to that of free fermions.

## 2. Regularized sine-Gordon theory

A systematic approach to incorporating lattice scale details into the sine-Gordon quench would require the inclusion of all irrelevant operators with a given scaling dimension, say. This task is made difficult by the interacting nature of most such operators. The problem is compounded by the fact that the influence of all irrelevant operators becomes strong in the ultraviolet, which

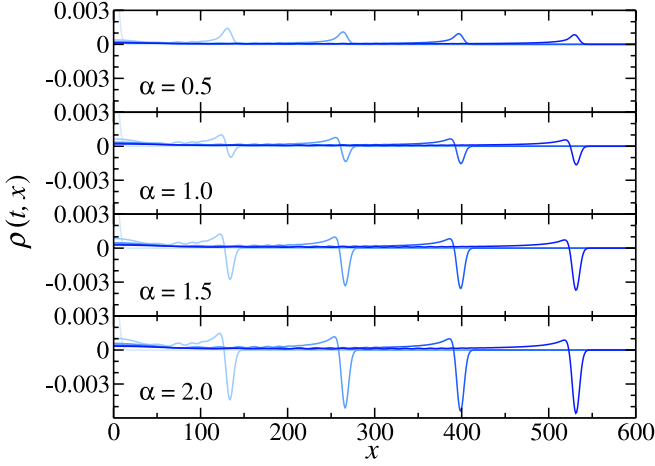


FIG. 9. The  $\zeta$ -regularized supersoliton obtained by numerically integrating Eq. (3.47). Here we have set  $\zeta = 1$ ,  $\Delta = 6$ , and plotted data for four values of  $\alpha$ . The interaction exponent  $\sigma = 0.7$ . We have assigned  $M = 3/2\Delta$ , so that the dynamics reside within the “non-relativistic” transport regime, as discussed in Sec. III A. For all but the smallest value  $\alpha$  depicted, the characteristic “s” shape of the supersoliton is identified at sufficiently long times. In comparison to the pure sine-Gordon model result shown in Fig. 6, the amplitude of the regularized supersoliton saturates at times  $t \gtrsim t_\zeta$ . Two inequivalent definitions for  $t_\zeta$  are provided by Eqs. (3.49) and (3.51).

is precisely the regime where lattice scale effects are expected to manifest.<sup>74</sup>

In the following, we sidestep these difficulties with a phenomenological approach. Compare the lattice and continuum initial state correlation functions  $\mathcal{C}(x_j, x_{j'})$  and  $\mathcal{C}^r_s(x_1, x_2)$  defined by Eqs. (2.13) and (3.14). While the long-distance behaviors of these functions should be compatible, the short-distance behaviors clearly differ. The continuum LL correlation functions in Eq. (3.20) exhibit a power-law divergence as  $x_1 \rightarrow x_2$  governed by twice the scaling dimension  $(\sigma + 1)/2$ ; by contrast, the lattice correlator satisfies  $\mathcal{C}(x_j, x_j) = \langle 0 | c_j^\dagger c_j | 0 \rangle = 1/2 + \mathcal{O}(Q)$ , independent of  $\sigma$  to lowest order. [ $|Q| \ll 1$  characterizes the small localized inhomogeneity induced by the chemical potential in Eq. (2.4).] To capture the effects of the lattice, we must cut off the divergence at zero argument in the continuum bosonization approximation to the *lattice* correlation function. We do this by incorporating a finite range  $\zeta$  associated with the nearest-neighbor density-density interactions in  $H^{(i)}$  [Eq. (2.3a)].

We obtain

$$\begin{aligned} \mathcal{C}(x_j, x_{j'}) &= \langle 0 | c^\dagger(x_j) c(x_{j'}) | 0 \rangle \\ &\sim \frac{c_N \alpha^\sigma}{\pi(x_j - x_{j'})} \left[ \frac{1}{(x_j - x_{j'})^2 + \zeta^2} \right]^{\sigma/2} \\ &\quad \times \sin \left[ k_F(x_j - x_{j'}) + \pi \int_{x_{j'}}^{x_j} dy \rho_0(y) \right], \end{aligned} \quad (3.46)$$

where  $\rho_0(y)$  denotes the initial density profile [Eq. (3.35)],  $c_N$  is the normalization constant from Eq. (3.20), and  $k_F = \pi/2$  is the Fermi wavevector at half-filling. In Eq. (3.35),  $K$  and  $u$  denote the Luttinger parameter and the sound velocity [for which we will employ the Bethe ansatz results in Eq. (2.5)]. To compare to the lattice quench, we use Eq. (2.7) for the exponent  $\sigma(\gamma)$ .

The correlator in Eq. (3.46) depends upon two length scales  $\alpha$  and  $\zeta$  not defined in the lattice theory. While the pure sine-Gordon model results from the limit  $\zeta \rightarrow 0$ , the parameter  $\alpha$  is always non-zero [c.f. Eq. (3.20)]; its evaluation in the context of the lattice model would require a Bethe ansatz calculation.<sup>1</sup> In comparing to numerics, we will fix  $\zeta = a = 1$  ( $a$  denotes the lattice spacing), consistent with nearest-neighbor interactions, but we will treat  $\alpha$  as a fitting parameter. Our choices for  $\zeta$  and  $\alpha$  will not prescribe the value  $\mathcal{C}(x_j, x_j) \equiv 1/2 + \mathcal{O}(Q)$ , except for the non-interacting quench  $\sigma = 0$ ; rather, we adjust  $\alpha$  to fit the long-range part of the correlator to the lattice numerics, since the regularized continuum approximation is still expected to behave the worst at short distances.

Incorporating the same  $\zeta$ -regularization into the component correlators in Eq. (3.20) and using the result in Eq. (3.13), one can analyze the “ultraviolet regularized” version of the sine-Gordon quench studied in the last section. The regularized post-quench density is expressed as the integral

$$\begin{aligned} \rho(t, x) &= \frac{1}{2} [\rho_0(x - t') + \rho_0(x + t')] \\ &\quad + \frac{c_N \alpha^\sigma}{\pi} \int_{-t'}^{t'} dy \frac{\sin \left[ \pi \int_{x-t'}^{x-y} dz \rho_0(z) \right]}{(t' - y) [\zeta^2 + (t' - y)^2]^{\sigma/2}} \bar{G}^{(1)}(t', y) \\ &\quad - \frac{c_N \alpha^\sigma}{\pi} \int_{-t'}^{t'} dy \frac{\sin \left[ \pi \int_{x+t'}^{x+y} dz \rho_0(z) \right]}{(t' + y) [\zeta^2 + (t' + y)^2]^{\sigma/2}} \bar{G}^{(3)}(t', y) \\ &\quad + \frac{c_N \alpha^\sigma}{2\pi} \int_{-t'}^{t'} dy_1 \int_{-t'}^{t'} dy_2 \frac{\sin \left[ \pi \int_{x-y_1}^{x-y_2} dz \rho_0(z) \right]}{(y_1 - y_2) [\zeta^2 + (y_1 - y_2)^2]^{\sigma/2}} \\ &\quad \quad \times \left[ \begin{aligned} &\bar{G}^{(1)}(t', y_1) \bar{G}^{(1)}(t', y_2) \\ &+ \bar{G}^{(3)}(t', y_1) \bar{G}^{(3)}(t', y_2) \\ &+ 2\bar{G}^{(2)}(t', y_1) \bar{G}^{(2)}(t', y_2) \end{aligned} \right], \end{aligned} \quad (3.47)$$

where  $\bar{G}^{(1,2,3)}(t, y)$  denote the unregularized continuum Green’s functions in Eq. (3.9); the primed time  $t' \equiv v_F t$  [Eq. (3.4)].



For interacting initial conditions  $\sigma > 0$  and  $\alpha$  not too small, the characteristic “s” shape of the supersoliton appears in the regularized sine-Gordon quench. The growth of the supersoliton amplitude is terminated after a certain cutoff time  $t_\zeta \propto \Delta/v_F(M\zeta)^2$  (discussed in more detail below). The regularized supersoliton is depicted in Fig. 9. Interpreting the sine-Gordon quench as the continuum limit of the lattice model version, we therefore anticipate the existence of at least three different dynamical regimes: (1)  $0 < t < 1/(v_F M)$ , transient regime, (2)  $1/(v_F M) < t < t_\zeta$ , “universal” supersoliton regime, (3)  $t > t_\zeta$ , post-cutoff, non-universal regime. These are sketched in Fig. 10.

To obtain an estimate for the cutoff time  $t_\zeta$ , we analyze the asymptotic behavior of the density response in Eq. (3.47). We can extract the first correction to Eq. (3.23) in the intermediate time window  $1/v_F M \ll t \ll t_\zeta$ ; the result is (c.f. Appendix A)

$$\begin{aligned} \rho(t, x) = & \frac{Q}{2\sqrt{\pi}\Delta} e^{-(x-t')^2/\Delta^2} \\ & - \frac{Q}{2\Delta} \frac{\Gamma(1-\sigma)}{\Gamma(\frac{1+\sigma}{2})} \left[ \frac{(M\alpha)^2 t'}{\sqrt{2}\Delta} \right]^{\sigma/2} \\ & \times \left[ \begin{array}{l} F_\sigma \left( \frac{x-t'}{\Delta} \right) \\ - \left[ \frac{(M\zeta)^2 t'}{\sqrt{2}\Delta} \right]^{\frac{1-\sigma}{2}} \frac{\Gamma(\frac{\sigma-1}{2})}{2\Gamma(-\sigma)} F_1 \left( \frac{x-t'}{\Delta} \right) \end{array} \right] \\ & + \{x \rightarrow -x\}, \end{aligned} \quad (3.48)$$

where the function  $F_\sigma(z)$  was defined by Eq. (3.24). The correction grows as  $t^{(1-\sigma)/2}$ , but with a sign opposite to the supersoliton. At intermediate times, the dominant effect is the suppression of the supersoliton growth. The expansion in Eq. (3.48) is a conserving approximation, because  $F_\sigma(z)$  integrates to zero ( $\sigma > 0$ ).

In the limit  $\sigma \rightarrow 0$ , the third term in Eq. (3.48) vanishes, as expected for the non-interacting quench (which is independent of  $\alpha$  and  $\zeta$ ). By contrast, ignoring the divergent prefactor we see that the second and third terms precisely cancel for  $\sigma = 1$ . This result obtains because the prediction of the unregularized sine-Gordon theory suffers a UV divergence for  $\sigma \geq 1$ ; a perturbative expansion about the  $\zeta = 0$  limit does not exist there.

We define  $f_1$  as the amplitude ratio of the second and third terms in Eq. (3.48), evaluated on the lightcone ( $x =$

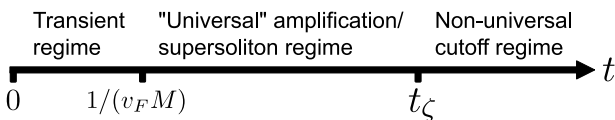


FIG. 10. Dynamical regimes of the lattice quench between  $H^{(i)}$  and  $H^{(f)}$  in Eq. (2.3), based on considerations of the regularized sine-Gordon model, as discussed in the text. The quench occurs at  $t = 0$ . The cutoff time  $t_\zeta$  can be defined by either Eq. (3.49) or (3.51).

$t'$ ). At argument  $z = 0$ ,  $F_\sigma(z)$  equals  $2^{\sigma/4}\sqrt{\pi}/\Gamma[(2-\sigma)/4]$ , a value close but not equal to its peak magnitude. For fixed ratio  $f_1$ , we then define the cutoff time

$$t_\zeta^{(1)} \equiv \frac{\Delta}{v_F(M\zeta)^2} \left[ \frac{2f_1 \Gamma(\frac{1}{4}) \Gamma(-\sigma)}{\Gamma(\frac{2-\sigma}{4}) \Gamma(\frac{\sigma-1}{2})} \right]^{2/(1-\sigma)}. \quad (3.49)$$

As an alternative, we compare the integral of the absolute values of the final two terms in Eq. (3.48). We define

$$\Omega_\sigma \equiv \int_{-\infty}^{\infty} dz |F_\sigma(z)|. \quad (3.50)$$

Eq. (3.50) can be evaluated numerically. Then, we set  $f_2$  equal to the ratio of the integrated absolute values associated with the second and third terms in Eq. (3.48). For fixed  $f_2$ , we have

$$t_\zeta^{(2)} \equiv \frac{\Delta}{v_F(M\zeta)^2} \left[ \frac{f_2 2^{(5-\sigma)/4} \Omega_\sigma \Gamma(-\sigma)}{\Omega_1 \Gamma(\frac{\sigma-1}{2})} \right]^{2/(1-\sigma)}. \quad (3.51)$$

Both  $t_\zeta^{(1,2)}$  diverge as  $\sigma \rightarrow 0$ , as expected for the non-interacting quench. Eqs. (3.49) and (3.51) are rapidly decreasing functions of  $\sigma$  that become ill-defined as  $\sigma \rightarrow 1$ . Unfortunately, both definitions are also strongly sensitive to the value that we assign to arbitrary ratio  $f_{1,2}$ . In particular, with  $\sigma = 0.4$  or  $0.7$ , for which we present lattice quench data in Sec. IV, the values of  $t_\zeta^{(1,2)}$  change by several orders of magnitude as  $f_{1,2}$  is swept from 0.1 to 1. The sensitivity reflects the very slow in time (fractional power law) accumulation of the final term relative to the second in Eq. (3.48). Thus, while the definition of a cutoff time with a natural scale  $\Delta/v_F(M\zeta)^2$  is conceptually useful, it proves difficult to utilize as a practical tool in characterizing finite-size numerics.

In the ultimate long-time limit  $t \gg t_\zeta$ , Eq. (3.47) has the leading asymptotic behavior (c.f. Appendix A)

$$\begin{aligned} \rho(t, x) \sim & \frac{Q}{2\sqrt{\pi}\Delta} \left[ 1 - \frac{\sqrt{\pi}\Gamma(1+\frac{\sigma}{2})}{\Gamma(\frac{1+\sigma}{2})} \left( \frac{\alpha}{\zeta} \right)^\sigma \right] e^{-(x-t')^2/\Delta^2} \\ & + \{x \rightarrow -x\}. \end{aligned} \quad (3.52)$$

In the regularized continuum quench, the supersoliton eventually gives way to a pure translation of the initial Gaussian, with a reduced amplitude. This is completely different from the single particle evolution resulting from “relativistic” confinement  $0 < M\Delta \ll 1$ , discussed in Sec. III A. In that case, the non-dispersive part of the amplitude decays to zero in the long time limit [Eq. (3.11)]. Eq. (3.52) is not a conserving approximation for any  $\sigma$ ; the missing density is distributed in a long tail neglected here. In fact, for  $\zeta = 1$  and  $\alpha \geq 0.64$ , the amplitude in Eq. (3.52) is *negative* for  $0 < \sigma < 1$ , which applies to Fig. 9. This is the case for the  $\sigma = 0.7$  and  $\sigma = 1.0$  quenches discussed in Sec. IV, although our lattice numerics are limited to system sizes much too small to reach this regime.

### 3. Band curvature lifetime

The sine-Gordon theory presented in the previous section accounts only for lattice effects on the *initial* pre-quench state, by way of the  $\zeta$ -regularized correlation function in Eq. (3.46). This is one ingredient in the post-quench evolution of the lattice density in Eq. (2.12); the other is the set of Green's functions  $G^{(1,2,3)}(t, x_i)$  obtained by Fourier-transforming Eq. (2.11). Instead, in Eqs. (3.47), (3.48), and (3.52), we have employed the continuum  $\tilde{G}^{(1,2,3)}(t, x)$  defined by Eq. (3.9), which assumes the Lorentz covariant spectrum in Eq. (3.26).

We find that this regularized correlator + continuum Green's functions approximation proves adequate to model most of the lattice quench numerics presented in Sec. IV. However, to characterize the dynamics in the limit of very long times (in a correspondingly large system), we would need to account for the additional effects of band curvature. This is of particular importance for the interacting quench, which yields the "regularized" supersoliton in Eq. (3.48) ( $t \ll t_\zeta$ ) or its ultimate fate as the non-dispersing ghost in Eq. (3.52) ( $t \gg t_\zeta$ ). These disturbances propagate at the "speed of light"  $v_F$ , which is replaced by the maximum band velocity  $v_{\max}(M)$  in the lattice model. [ $v_{\max}(0) = v_F$ ; see Sec. IV B 2 for more details.] As a first correction to the continuum dynamics, we consider the cubic curvature represented by  $\mathcal{O}_3$  in Eq. (3.41).

The lifetime  $t_3$  is defined as the interval post-quench during which the cubic curvature can be *ignored*; a crude order-of-magnitude estimate is given by

$$t_3 \sim \frac{\Delta^3}{v_{\max}(M)}, \quad (3.53)$$

where  $\Delta$  is the position space width of the initial density inhomogeneity. Eq. (3.53) follows from the expansion of the band dispersion in Eq. (2.6) about  $k_{\max}$  such that  $v(k_{\max}) = v_{\max}$  (Sec. IV B 2):

$$E_k = E_{k_{\max}} + v_{\max} \left[ \delta k - \frac{2}{3} a^2 \delta k^3 \right] + \dots$$

where  $\delta k \equiv k - k_{\max}$ ;  $a$  is the lattice constant. For a Gaussian packet of width  $\Delta$ , the characteristic frequency associated to the cubic term is  $v_{\max} a^2 / \Delta^3$ , giving Eq. (3.53) with  $a = 1$ .

## IV. LATTICE QUENCH RESULTS

In this section, we present numerical results for the XXZ chain quench set up in Sec. II. A chain with  $N$  (even) sites and periodic boundary conditions is prepared in the ground state  $|0\rangle$  of  $H^{(i)}$ , Eq. (2.3a). The interaction strength  $\gamma$  is chosen to reside in the XY range  $-1 < \gamma \leq 0$ , so that  $|0\rangle$  exhibits gapless power-law correlations for the lattice fermions. This state is evolved forward in time according to  $H^{(f)}$ , Eq. (2.3b).

For the Gaussian initial state inhomogeneity induced by  $\mu_i^{(0)}$  in Eq. (2.4), we calculate the post-quench dynamics of the density expectation value  $\rho(t, x)$ , Eq. (2.12). In the generic case of the interacting quench ( $\gamma \neq 0$ ), the required initial state correlation function  $\mathcal{C}(x_j, x_{j'})$  is computed numerically using the density matrix renormalization group (DMRG) technique. All data shown are for a system of  $N = 202$  sites.

We compare the numerical results for the lattice quench to the regularized continuum sine-Gordon theory presented in Sec. III D 2. That theory is epitomized by the continuum approximation to the initial state lattice correlation function in Eq. (3.46) and the density expectation in Eq. (3.47). The regularized sine-Gordon model contains two length scale parameters  $\alpha$  and  $\zeta$  that are not defined in the corresponding lattice theory. These parameters enter via the initial state correlation function  $\mathcal{C}(x_j, x_{j'})$  in Eq. (3.46). The parameter  $\alpha$  determines the amplitude of this correlator, while  $\zeta$  acts as an ultraviolet cutoff that renders finite the on-site value of  $\mathcal{C}(x_j, x_j)$ . For the non-interacting quench ( $\sigma = 0$ ), the continuum predictions are independent of  $\zeta$  and  $\alpha$ .

### A. Non-interacting quench

The special case  $\gamma = 0$  yields a free Fermi gas ground state of  $H^{(i)}$ . Both the initial and final Hamiltonians are trivially diagonalized, and we solve for the dynamics exactly. For this "non-interacting" quench, the initial state correlation function was transcribed in Eq. (2.14), above.

We first investigate the quench into the gapless XX chain,  $M = 0$  in  $H^{(f)}$ . Since the low-energy field theory description of both the initial and final states is a free Fermi gas, we refer to this as a "FG to FG" quench. Thus one prepares a density wavepacket at the origin, then simply removes the applied potential and tracks the resulting dynamics. Numerical results are depicted in Figs. 11 and 12 for two different values of  $\Delta$ .

The continuum prediction is a pure translation of half the initial density profile to the left and to the right, at the "speed of light"  $v_F = 2$ . The right-moving part appears as the first term on the right-hand side of Eq. (3.48). One can see in Figs. 11 and 12 that the agreement between the continuum and the lattice quenches is very good, and improves with increasing  $\Delta$ . The slight dispersion seen for  $\Delta = 4$  in Fig. 11 can likely be attributed to the deviation of the band spectrum [Eq. (2.6) with  $M = 0$ ] from linearity at wavenumbers  $k \sim 1/\Delta$  away from the Fermi wavevector  $k_F = \pi/2$ . As discussed in Sec. III D 3, we can associate a lifetime  $t_3 \sim \Delta^3/v_F$  to the presence of the cubic non-linearity in the spectrum. Then  $t_3(\Delta = 12) \sim 860$ , while  $t_3(\Delta = 4) \sim 32$ ; the latter falls midway in the range of times plotted in Fig. 11.

We now turn to non-interacting quenches into a *gapped* final Hamiltonian. Here, we quench from a free Fermi gas into a band insulator. The periodic potential in

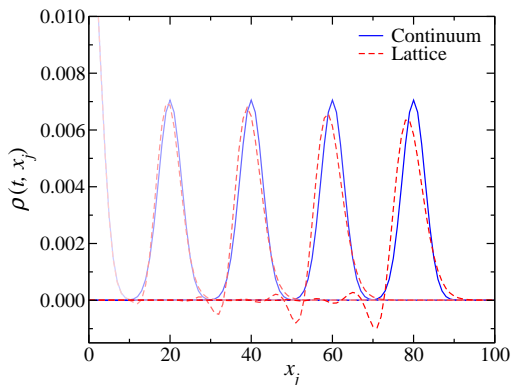


FIG. 11. Time slices of a non-interacting quench with a gapless final Hamiltonian [ $M = 0$  in Eq. (2.3b), a “Fermi gas to Fermi gas” quench] at times  $t = 0, 15, 30, 45$ , and  $60$ ; fainter (bolder) traces depict earlier (later) times. Blue solid lines are the continuum prediction [the first term of Eq. (3.48)], and red dashed lines are the result of exact diagonalization of the lattice Hamiltonian. The evolution is symmetric about  $x_j = 0$ . The relevant quench parameters are  $Q = 0.10$ ,  $\Delta = 4$ .

Eq. (2.3b) with  $M \neq 0$  allows for backscattering umklapp processes, which open up a bandgap with magnitude  $4M$ . To compare to the continuum theory, we would like to reach the scaling limit where all relevant length scales in the problem greatly exceed the lattice spacing, e.g.  $\Delta \gg a$ ,  $1/M \gg a$ , while keeping  $\Delta \ll Na$ . In addition, we restrict our quench parameters to the “non-relativistic” transport regime  $M\Delta > 1$ , as explained in Sec. III A, so as to avoid confusing the putative supersoliton (in the interacting quench, below) with relativistic propagation induced by excessive “squeezing” of the initial density disturbance relative to the Compton wavelength. Specifically, for all data presented subsequently we will fix the product  $M\Delta = 3/2$ , and examine four wavepacket widths  $\Delta = 4, 6, 12$ , and  $20$ , yielding the respective band-gap parameters  $M = 3/8, 1/4, 1/8$ , and  $3/40$ .

The application of the staggered potential causes adjacent site occupancies to ‘polarize’ opposite to one an-

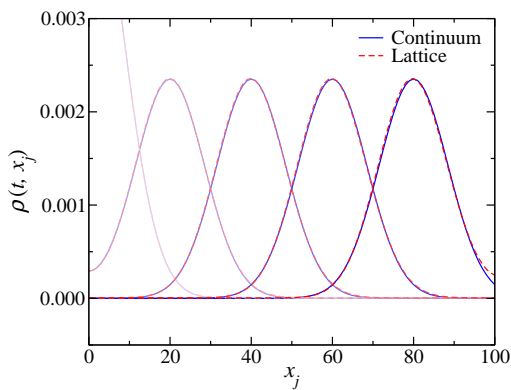


FIG. 12. The same as in Fig. 11, but with  $\Delta = 12$ .

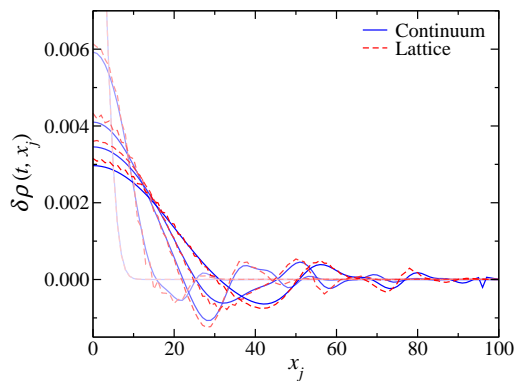


FIG. 13. Time slices of a non-interacting quench into a gapped final Hamiltonian (a non-interacting Fermi gas to band insulator quench) at times  $t = 0, 15, 30, 45$ , and  $60$ ; fainter (bolder) traces depict earlier (later) times. Blue solid lines are the continuum predictions and red dashed lines are the result of exact diagonalization of the lattice Hamiltonian. The continuum data results from a numerical integration of Eq. (3.47) with  $\sigma = 0$ . The evolution is symmetric about  $x_j = 0$ . The relevant quench parameters are  $Q = 0.10$ ,  $\Delta = 4$ ,  $M = 3/8$ .

other, but this small-scale density effect is not one in which we are interested; the staggered potential is merely a tool to induce a gap in the spectrum. We henceforth present results for the *relative* particle density, given by

$$\delta\rho(t, x_j) \equiv \rho(t, x_j)_Q - \rho(t, x_j)_{Q=0}, \quad (4.1)$$

i.e. we subtract the time-dependent density profile originating from a spatially homogeneous ( $Q = 0$ ) initial state.

Figs. 2 (in the Introduction) and 13 show the resulting post-quench dynamics for two of the four  $(\Delta, M)$  pairs given above. The dynamics are strongly dispersive, in stark contrast to the ultrarelativistic propagation seen in the FG to FG quench. We see that the initial Gaussian inhomogeneity broadens gradually and does so more slowly for larger values of the band gap; these non-interacting quench dynamics are grossly similar to the non-relativistic single particle wavepacket depicted in Fig. 5(a). The behavior is generic and we find it to occur for a wide range of non-interacting quench parameters satisfying the non-relativistic condition  $M\Delta > 1$ .

The dispersion arises from a combination of the strong band curvature near the (non-interacting) Fermi point and the relatively weak occupancy of the conduction band induced by the quench, as evidenced by the corresponding distribution function plots in Fig. 8 with  $\sigma = 0$ . We emphasize however that the global momentum distribution in Fig. 8 does not encode information about the inhomogeneity; for this purpose one should consult the Wigner function, as discussed in Sec. III C 2 and Appendix C. For the continuum theory, we find that the “local” velocity distribution for the non-relativistic, non-interacting quench exhibits a strong suppression of velocities  $v \gtrsim v_F/M\Delta$  [Eq. (C7) in Appendix C], due

to Pauli-blocking in the initial Fermi gas ground state (Sec. III C 2).

The continuum curves in Figs. 2 and 13 obtain from the numerical integration of Eq. (3.47), with  $\sigma = 0$ . The agreement between the lattice and continuum quench dynamics is generally excellent. For the  $\Delta$  values considered, we observe negligible sublattice staggering in the lattice  $\delta\rho(t, x_j)$ ; such behavior is a good indicator of the near complete separation of the smooth and staggered components of the density. This is consistent with the retention of only the smooth component of the initial inhomogeneity in the regularized sine-Gordon theory of Sec. III D 2.<sup>54</sup>

## B. Interacting quench

We turn to the most interesting case of an *interacting* initial state,  $\gamma \neq 0$  in Eq. (2.3a). Because the final state is still non-interacting, the dynamics are exactly given by Eq. (2.12) above, but the initial state correlation function  $\mathcal{C}(x_j, x_{j'})$  cannot be obtained via elementary means. To achieve this task, we employ the density matrix renormalization group (DMRG)<sup>75–77</sup> due to its ability to treat relatively large interacting one-dimensional systems. All calculations were performed on a chain of size  $L = 202$  (so that the number of fermions at half-filling,  $L/2$ , is odd) with periodic boundary conditions (PBCs). In standard DMRG, the relative error introduced with PBCs is significantly larger than that obtained with open boundary conditions (OBCs). To achieve the relative error obtained with  $m$  states per block using OBCs, one would need  $m^2$  states when using PBCs. This results in greatly increased computational times which scale as  $m^6$  with PBCs as compared to  $m^3$  with OBCs. Efficient methods to improve DMRG's ability to handle PBCs are still ongoing topics of research (see e.g. Ref. 78 and references therein). In spite of the above considerations, we found the use of PBCs was necessary to mitigate dynamical boundary effects appearing during the quench process. In all calculations presented, we kept up to 200 states and performed eight sweeps in the DMRG algorithm, yielding a truncation error (discarded weight) on the order of  $10^{-7}$ . We tested the combination of DMRG and exact time evolution for the non-interacting quench by comparing to the results of exact diagonalization, presented in the previous section.

Although our DMRG calculations are complicated by the use of PBCs and a spatially inhomogeneous Hamiltonian, one could in principle imagine performing DMRG calculations for larger systems. Unfortunately, although the (non-interacting) dynamics are trivially written down, they suffer from quite poor polynomial scaling with system size. Namely, forward and backward Fourier transforms [each requiring  $O(N)$  operations] for each of the  $N$  sites out to times scaling with the size of the system yields a dynamics algorithm which scales as  $O(N^4)$ . Calculating the dynamics for systems

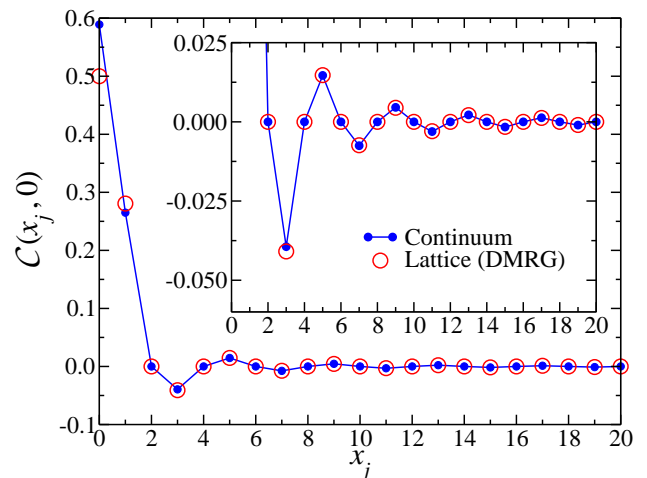


FIG. 14. Comparison of the initial state correlation function  $\mathcal{C}(x_j, 0)$  defined in Eq. (2.13), as predicted by the regularized ( $\alpha = 0.75$ ,  $\zeta = 1$ ) LL theory [Eq. (3.46), blue dots connected by lines] and as calculated with DMRG (red open circles). The inset is a close-up of the same data. The relevant parameters are  $\sigma = 1.0$ ,  $Q = 0.0$ .

much larger than those considered here is currently prohibitive.

### 1. Initial state correlator

As a first analysis, we consider the initial state correlation function  $\mathcal{C}(x_j, 0)$  [Eq. (2.13)]. LL theory predicts interaction-dependent power-law behavior in correlation functions. At large separations, Eq. (3.46) yields

$$\mathcal{C}(x_j, 0) \sim |x_j|^{-(\sigma+1)}, \quad (4.2)$$

where the exponent  $\sigma$  is taken as the Bethe ansatz result, Eq. (2.7). Fig. 14 compares the correlation function cal-

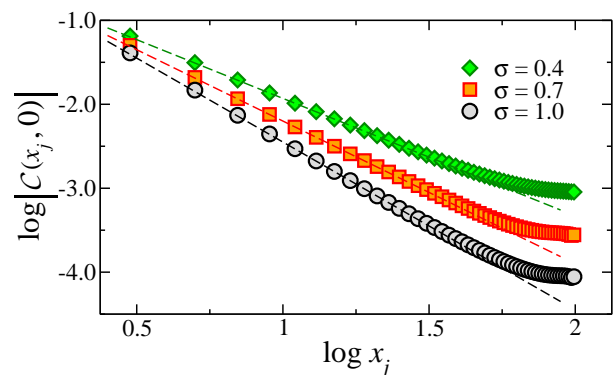


FIG. 15. Envelopes of the correlation function  $\mathcal{C}(x_j, 0)$  calculated by DMRG for the dynamical exponents  $\sigma = 1.0$  (black circles),  $0.7$  (red squares), and  $0.4$  (green diamonds) – all for  $Q = 0.0$ . The dashed lines are a guide to the eye, exhibiting slopes  $-2$ ,  $-1.7$ , and  $-1.4$  (bottom to top).

culated numerically by DMRG to the regularized continuum prediction for  $\sigma = 1.0$ , with  $Q = 0$ . [For the cases of non-zero inhomogeneity with small  $|Q|$  considered below, the  $Q$ - and  $\Delta$ -dependencies of  $\mathcal{C}(x_j, x_{j'})$  are very minor.] To fix the continuum result in Eq. (3.46), we make the physically motivated choice  $\zeta = a = 1$ , associated with nearest-neighbor density-density interactions on the lattice, while we adjust the scale-setting prefactor  $\alpha$  to best match the DMRG calculated correlation function at *large* separations. This approach yields  $\sigma$ -dependent values of  $\alpha$ , specifically  $\alpha = 0.75, 0.64$ , and  $0.50$  for  $\sigma = 1.0, 0.7$ , and  $0.4$ , respectively. The agreement between the lattice and continuum correlation functions is seen in Fig. 14 to be excellent after such a fitting procedure; similar agreement is obtained for the other values of  $\sigma$ . The regularization parameters obtained in this manner are also employed in the subsequent continuum calculation of the interacting quench dynamics.

The power-law prediction emerging from LL theory is seen to be very robust. In Fig. 15, we plot (in log-log scale) the envelope of the DMRG correlation function for the interaction strengths yielding exponents  $\sigma = 1.0, 0.7$ , and  $0.4$ . The deviations occurring at the largest separations are an artifact of the numerics.

## 2. Maximum band velocity

Below we compute the quench dynamics originating from an interacting initial state characterized by the correlation function analyzed above. We first pause to discuss a time-rescaling procedure adopted in the following. In Sec. III C 1, we considered the static post-quench distribution functions  $n_{\pm}(k)$  for conduction and valence band fermions [excitations of the final band insulating Hamiltonian  $H^{(f)}$  or  $\bar{H}^{(f)}$ ] in the lattice and continuum quenches. Continuum results for the non-interacting and interacting quenches are given by Eqs. (3.31) and (3.33). Fig. 8 shows lattice quench results for  $n_{+}(k)$  obtained from the DMRG initial state correlation function associated with the four values of  $M$  considered in this section. Each subplot exhibits traces for  $\sigma = 0, 0.4, 0.7$ , and  $1.0$ .

Fig. 8 indicates that the final state distribution of excited particles for an interacting quench ( $\sigma > 0$ ) extends deep into the conduction band. Although the final particle spectrum in Eq. (2.6) is quadratic at low energies near the band center, the distribution induced by an interacting quench stretches into the linear “relativistic” regime of the spectrum and beyond. In the ungapped case, the slope  $v_F = 2$  for  $k$  just above  $k_F = \pi/2$ ; with  $M > 0$ , the maximum group velocity of the band structure is modified to  $v_{\max}(M) < 2$ . It is this velocity with which we henceforth rescale time in the continuum calculations,  $t' = v_{\max}(M)t$  in Eq. (3.47).

For  $E_k$  in Eq. (2.6), the velocity  $v(k; M) \equiv dE_k(M)/dk$  evaluates to

$$v(k; M) = -\frac{2 \sin(k) \cos(k)}{\sqrt{\cos^2(k) + M^2}}. \quad (4.3)$$

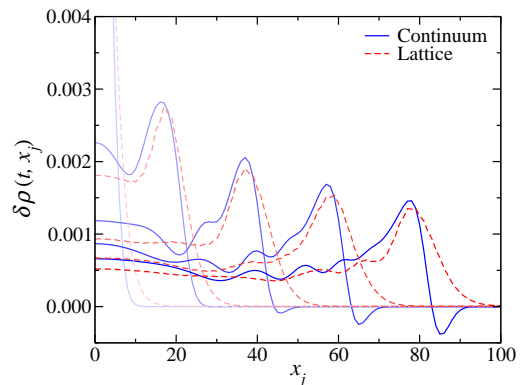


FIG. 16. Time slices of an interacting quench with  $\sigma = 1.0$  into a gapped final Hamiltonian (an interacting Luttinger liquid to band insulator quench) at times  $t = 0, 15, 30, 45$ , and  $60$ ; fainter (bolder) traces depict earlier (later) times. Blue solid lines are the continuum predictions and red dashed lines are the results of DMRG calculations combined with exact time evolution of the lattice Hamiltonian. The continuum data obtains from a numerical integration of Eq. (3.47), with  $\alpha = 0.75$  and  $\zeta = 1$ . The evolution is symmetric about  $x_j = 0$ . The relevant quench parameters are  $Q = 0.10$ ,  $\Delta = 4$ ,  $M = 3/8$ .

This equation is maximized at a wavevector  $k_{\max}$  satisfying

$$\cos(k_{\max}) = \sqrt{\sqrt{M^2 + M^4} - M^2}. \quad (4.4)$$

Inserting the solution of Eq. (4.4) into Eq. (4.3) yields the maximal band velocity  $v_{\max}(M)$ . In Fig. 8, the position of  $k_{\max}$  for each value of  $M$  is indicated by a dashed vertical line.

The velocity rescaling procedure outlined above was *not* adopted in the continuum non-interacting quench data exhibited in Figs. 2 and 13. For the case  $\sigma = 0$ , Fig. 8 indicates that the linear regime is only weakly populated for all but the largest value of  $M = 3/8$  considered here; see also Eq. (3.31). As a consequence, the strongly dispersive dynamics in the “non-relativistic” transport regime  $M\Delta > 1$  are dominated by the low- $k$  bandstructure. This picture is confirmed by the excellent agreement between lattice and continuum results in Figs. 2 and 13, and by the local velocity distribution obtained for the non-interacting, non-relativistic quench in Eq. (C7). For the interacting quenches considered below, the rescaling of the velocity is not a systematic incorporation of bandstructure effects into the continuum Green’s functions defined by Eq. (3.9); aspects of ultraviolet band curvature beyond the linear regime have been neglected. Band curvature effects are expected to become important at post-quench times  $t$  later than  $t_3$ , defined as the cubic dispersion lifetime via Eq. (3.53).

## 3. Coherent relativistic wave propagation:

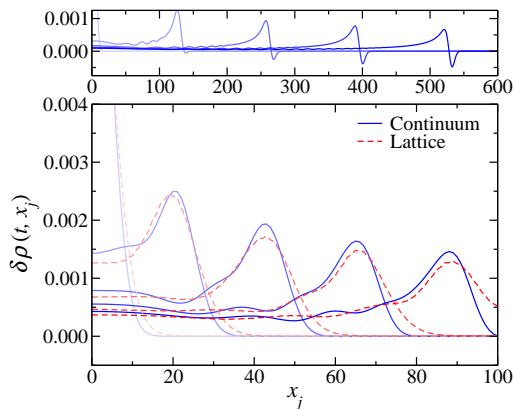


FIG. 17. Interacting quench with  $\sigma = 1.0$  as in Fig. 16, but with  $\Delta = 6$ ,  $M = 1/4$ . The continuum result [numerical integration of Eq. (3.47)] can be obtained for much larger times and system sizes than is currently practical with the interacting numerics (DMRG+dynamics). The top panel shows the continuum evolution over a window of length 600.

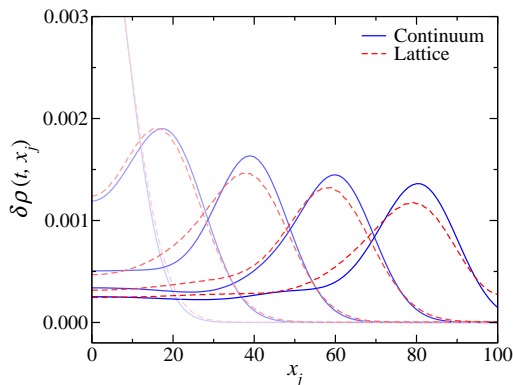


FIG. 18. Interacting quench with  $\sigma = 1.0$  as in Fig. 16, but at times  $t = 0, 12, 24, 36,$  and  $48$ , with  $\Delta = 12$ ,  $M = 1/8$ .

#### *the “regularized” supersoliton*

In Figs. 16-24 we present the interacting quench dynamics associated with three different values of the exponent  $\sigma(\gamma)$  defined by Eq. (2.7), which characterizes the initial interacting spin chain described by  $H^{(i)}$ . The values we choose are  $\sigma = 1.0$  (Figs. 16–19),  $\sigma = 0.7$  [Figs. 20, 21, and 1 (in the Introduction)], and  $\sigma = 0.4$  (Figs. 22–24); these respectively correspond to interaction strengths  $\gamma = -0.913, -0.872,$  and  $-0.790$ , receding from the ferromagnetic transition at  $\gamma = -1$  (Fig. 4). In the unregularized, pure sine-Gordon theory described in Ref. 43 and in Sec. III B, the quench yields the prediction of the supersoliton for  $0 < \sigma < 1$  [Eq. (3.23) and Fig. 6], while  $\sigma = 1$  marks the onset of an ultraviolet divergence that must be regularized, as in Eq. (3.46).

We show data for  $\Delta = 4, 6, 12,$  and  $20$  in Figs. 16–19, respectively; except for  $\Delta = 20$ , the same values appear in Figs. 1 and 20–24. We emphasize that all quenches have  $M = 3/2\Delta$ , the same relationship imposed

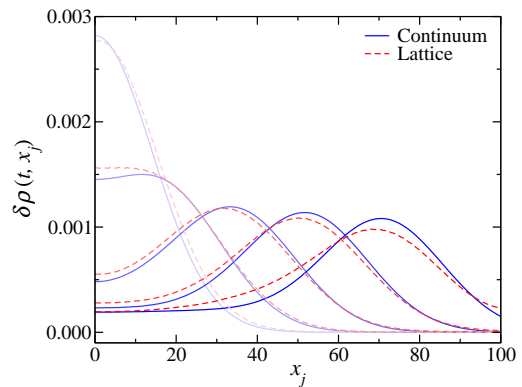


FIG. 19. Interacting quench with  $\sigma = 1.0$  as in Fig. 16, but at times  $t = 0, 10, 20, 30,$  and  $40$ , with  $\Delta = 20$ ,  $M = 3/40$ .

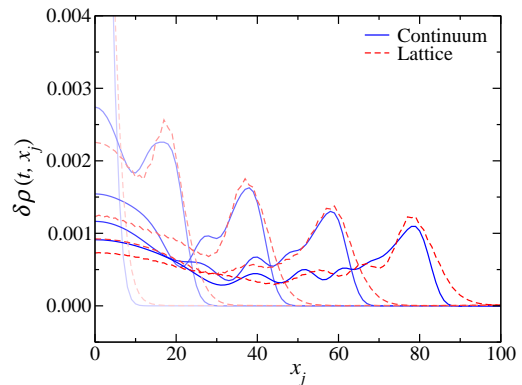


FIG. 20. Time slices of an interacting quench with  $\sigma = 0.7$  at times  $t = 0, 15, 30, 45,$  and  $60$ . The continuum data obtains from a numerical integration of Eq. (3.47), with  $\alpha = 0.64$  and  $\zeta = 1$ . The relevant quench parameters are  $Q = 0.10$ ,  $\Delta = 4$ ,  $M = 3/8$ .

for the non-interacting case. This constraint puts all of our quenches in the “non-relativistic” transport regime, as discussed in Sec. III A. A single particle wavepacket with  $M\Delta = 3/2$  shows only slow broadening, similar to the non-interacting quench data in Figs. 2 and 13.

The difference in density dynamics for the interacting quenches shown in Figs. 1 and 16-24 as compared to the non-interacting versions in Figs. 2 and 13 is remarkable. For all interacting parameter sets investigated, we observe a strong separation of dispersive dynamics localized near the origin (the center of the chain and of the initial Gaussian inhomogeneity), and well-defined left- and right-moving wavepackets that propagate away from the origin showing minimal dispersion in their spatial extents. [Only the right-moving packet is depicted; the left-mover is an exact mirror image for the Gaussian initial condition in Eq. (2.4).] Furthermore, we find empirically that these wavepackets travel “relativistically,” i.e. at the maximal band velocity  $v_{\max}(M)$  determined above. By tracking the peak of the right-moving wavepacket, we are able to extract its propagation speed, which we plot in Fig. 25 on top of  $v_{\max}(M)$ . The error bars shown there

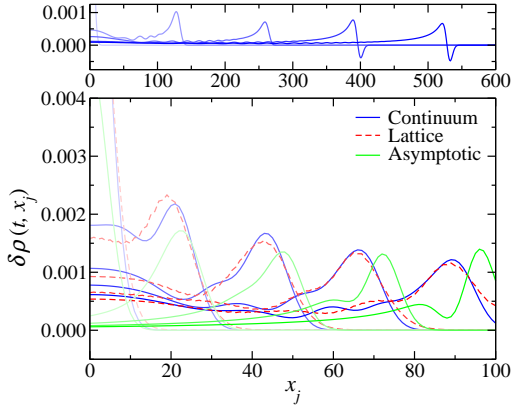


FIG. 21. Interacting quench with  $\sigma = 0.7$  as in Fig. 20, but with  $\Delta = 6$ ,  $M = 1/4$ . The curve marked “asymptotic” is the analytical result for the “regularized supersoliton” in Eq. (3.48). The top panel shows the numerical continuum evolution over a window of length 600.

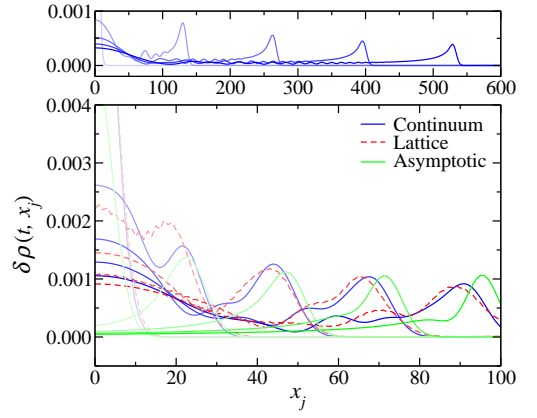


FIG. 23. Interacting quench with  $\sigma = 0.4$  as in Fig. 22, but with  $\Delta = 6$ ,  $M = 1/4$ . The curve marked “asymptotic” is the analytical result for the “regularized supersoliton” in Eq. (3.48). The top panel shows the numerical continuum evolution over a window of length 600.

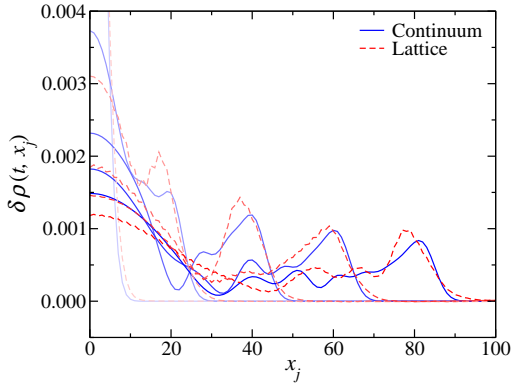


FIG. 22. Time slices of an interacting quench with  $\sigma = 0.4$  at times  $t = 0, 15, 30, 45$ , and  $60$ . The continuum data obtains from a numerical integration of Eq. (3.47), with  $\alpha = 0.50$  and  $\zeta = 1$ . The relevant quench parameters are  $Q = 0.10$ ,  $\Delta = 4$ ,  $M = 3/8$ .

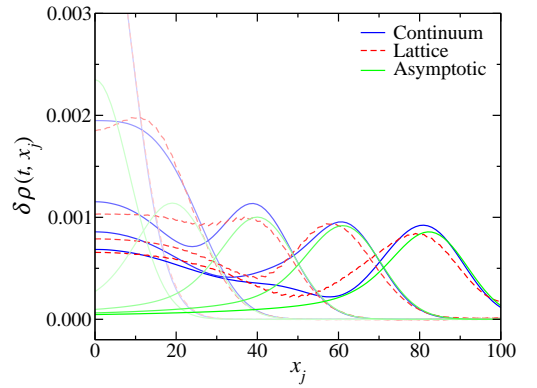


FIG. 24. Interacting quench with  $\sigma = 0.4$  as in Fig. 22, but at times  $t = 0, 12, 24, 36$ , and  $48$ , with  $\Delta = 12$ ,  $M = 1/8$ . The curve marked “asymptotic” is the analytical result for the “regularized supersoliton” in Eq. (3.48).

originate solely from the linear fit (of peak position vs. time). The deviation seen at low  $M$  (wide  $\Delta$ ) for weak interaction strengths likely originates from the inaccuracy in determining the exact peak location of such a shallow, wide wavepacket as well as from possible transient distortion of the wavepacket’s shape over its initial time evolution.

The continuum data in Figs. 16-24 was obtained by integrating the regularized sine-Gordon result in Eq. (3.47) numerically, using  $\zeta = 1$  and the values of  $\alpha$  quoted in the figure captions. Because the velocity renormalization scheme employed does not represent a fully systematic incorporation of lattice dispersion details into the continuum Green’s functions in Eq. (3.9), we anticipate poorest agreement between lattice and continuum data in the dispersive “tail” dynamics occurring near the origin. By contrast, we find very good agreement for the propagating wavepacket’s speed and overall shape, despite the

crude phenomenological regularization of the continuum initial state correlator.

The largest discrepancies between continuum and lattice predictions occur for the smallest  $\Delta = 4$ , and are particularly pronounced in the parameter set ( $\sigma = 1.0$ ,  $\Delta = 4$ ,  $M = 3/8$ ), Fig. 16. A significant deviation for  $\Delta = 4$  is also observed in the non-interacting,  $M = 0$  quench shown in Fig. 11. Taken together, these results suggest that band curvature at the ultraviolet scale  $k \sim k_{\max}(M) + 1/\Delta$  becomes important in the lattice quench for this case. This behavior is not accounted for in our continuum calculations, which instead assume the massive Dirac fermion spectrum  $\varepsilon_k = v_{\max}(M)\sqrt{k^2 + M^2}$  for the final state Hamiltonian  $\bar{H}^{(f)}$ , Eq. (3.1) (here  $k$  is measured relative to  $k_F$ ). For  $\Delta = 4$ , the cubic curvature lifetime in Eq. (3.53)  $t_3 \sim \Delta^3/v_{\max}(M) = 46$ , within the range of plotted time slices in Fig. 16. For  $\Delta = 6$ , our estimate for  $t_3$  leaps to 140.

What can we say about the supersoliton identified in

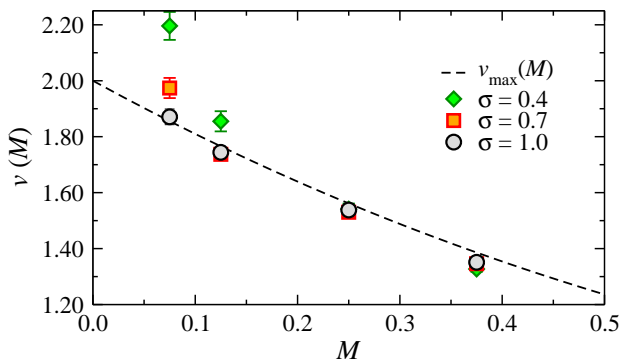


FIG. 25. The maximum band velocity versus the band gap parameter,  $M$ , as calculated by Eqs. (4.3) and (4.4) [black dashed line] and the propagation velocity of the relativistically moving wavepacket in the interacting lattice quench for the values  $\sigma = 0.4$  [green diamonds],  $0.7$  [red squares], and  $1.0$  [black circles].

the unregularized, continuum sine-Gordon quench studied in Ref. 43, reviewed in Sec. III B? The supersoliton is defined as the asymptotic, long time ( $t \gg 1/v_F M$ ) result for the pure sine-Gordon model transcribed in Eq. (3.23), exhibited in Fig. 6. The supersoliton propagates ultrarelativistically at the “speed of light”  $v_F$ , has a particular, non-dispersing “s” shape and an amplitude that grows in time as  $t^{\sigma/2}$ . As articulated in Sec. III C 2, the supersoliton arises due to quasiparticle *fractionalization*. Fractionalization of the initial, interacting LL state relative to the gas of propagating post-quench fermions induces a power-law excitation of large momenta in the “local” Wigner distribution function  $n(k; R)$ , as exemplified in Eq. (3.39). By contrast, in the non-interacting quench momenta  $|k| \gg 1/\Delta$  are exponentially suppressed as a consequence of Pauli-blocking (Sec. III C 2). Through the massive post-quench dispersion, the Wigner function translates into a “local” velocity distribution. In the non-interacting quench with  $M\Delta \gg 1$ , only small velocities  $v \lesssim v_F/M\Delta$  are significantly excited [Eq. (C7) in Appendix C]; in the interacting case, a non-integrable divergence appears at the “speed of light”  $v_F$  [Eq. (C8a)], irrespective of  $M\Delta$ , signaling the presence of the supersoliton. Although regularization of the LL correlation functions  $\mathcal{C}_s^r(x, x')$  in Eqs. (3.20) or (3.46) at short distances ultimately cuts off this divergence [Eq. (C8b)], the distinction between the interacting and non-interacting quenches survives, because the power-law behavior in  $\mathcal{C}_s^r(x, x')$  at *large* distances is enough to undermine Pauli-blocking, for  $\sigma > 0$ .

In the XXZ lattice quench studied here, we do not observe the characteristic “s” shape of the supersoliton in any of the lattice data. In particular, the density fluctuation  $\delta\rho(t, x_j)$  appears strictly positive for the interacting quenches, although negative excursions are observed for non-interacting quenches, Figs. 2 and 13. In each Fig. 17, 21, and 23 ( $\sigma = 1.0, 0.7$ , and  $0.4$ , respectively, all with  $\Delta = 6$ ), the slim upper panel shows the continuum evolu-

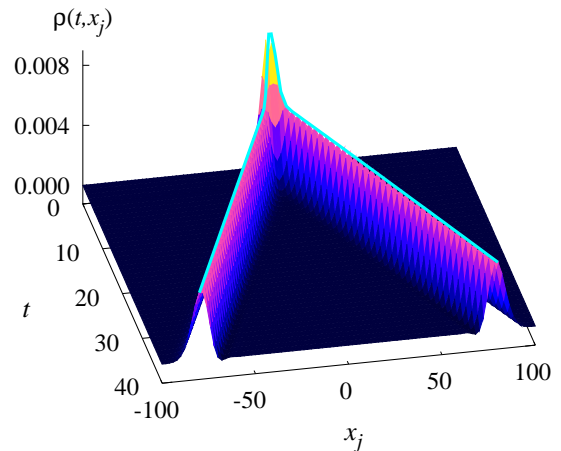


FIG. 26. Three dimensional view of the Fermi gas to Fermi gas lattice quench ( $\sigma = 0, M = 0$ ) with  $Q = 0.1, \Delta = 6$ . The cyan line demarks the maximal propagation speed,  $v_{\max} = v_F = 2$ .

tion [numerical integration of Eq. (3.47)] over a window of length 600, corresponding to a system size 6 times larger than that used for the lattice quench. For  $\sigma = 1.0$  and  $0.7$ , the continuum data shows the emergence of a negative peak at times and positions much larger than could be accessed in the numerical lattice study. The relatively good agreement between the lattice and continuum results over the 100-site windows in Figs. 17 and 21 suggests the possibility that the “s”-shape can appear in the lattice quench, but only larger system size studies can resolve this question.<sup>79</sup>

A more precise way to analyze the interacting lattice quench data is to employ Eq. (3.48). This equation describes a type of “regularized” supersoliton that appears at intermediate timescales: the first two terms are the pure sine-Gordon theory result, while the third term is the first correction due to a non-zero ultraviolet regularization parameter  $\zeta$ . Eq. (3.48) obtains from asymptotic analysis of the “exact” regularized sine-Gordon result in Eq. (3.47), valid for  $v_F M \ll t \lesssim t_\zeta$  and  $0 < \sigma < 1$ ; see also Fig. 10. The cutoff time  $t_\zeta \propto \Delta/v_F(M\zeta)^2 \propto \Delta^3$  (since  $M\Delta = 3/2$  here); alternative definitions of the  $\sigma$ -dependent proportionality constant are provided in Eqs. (3.49) and (3.51). In Figs. 1, 21, 23, and 24, we have included time series plots of Eq. (3.48) for the quench parameters transcribed in the captions. For  $\Delta = 12$ , Figs. 1 and 24, there is rough agreement between the asymptotic result, the lattice quench, and the numerical continuum integration for the latest time steps plotted. Eq. (3.48) fails at earlier times, where transient behavior dominates both the lattice and continuum. The asymptotic result does not fare as well for  $\Delta = 6$ , Figs. 21 and 23, although the lattice data is well-modeled by the numerical integration of Eq. (3.47). Since the cutoff time  $t_\zeta \sim \Delta^3$ , the failure of Eq. (3.48) for smaller values of  $\Delta$  indicates the need to retain higher order terms in this expansion; the closest agreement between Eq. (3.48) and the lattice



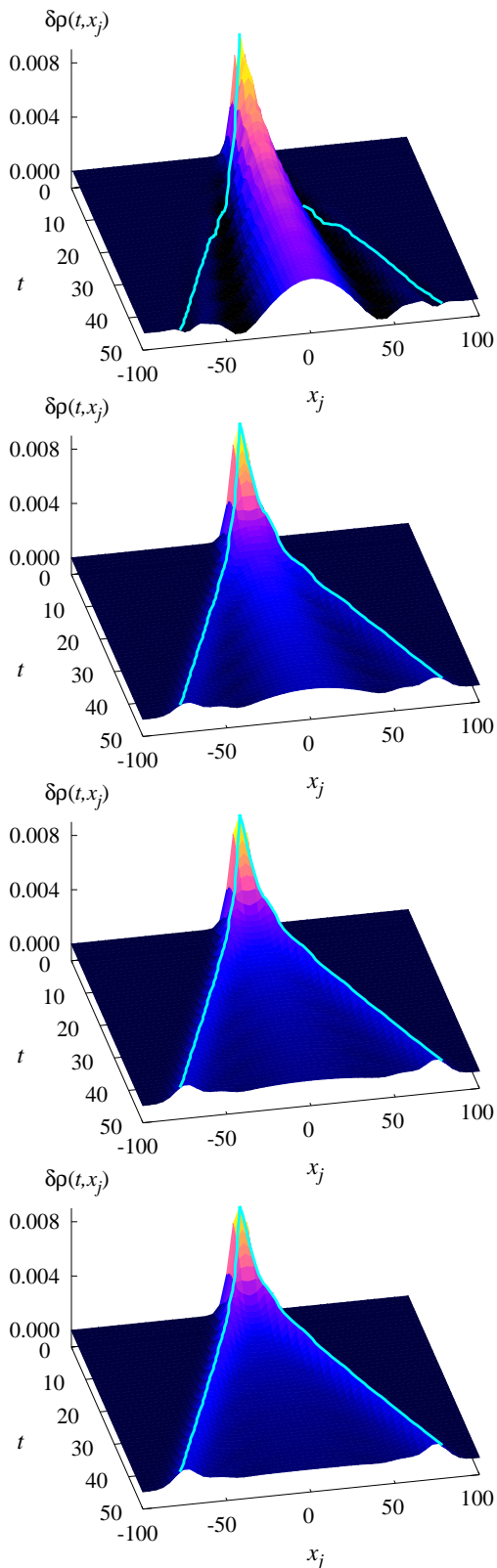


FIG. 27. Three dimensional view of lattice quenches with  $Q = 0.1$  and  $\Delta = 6$ , into a gapped final Hamiltonian with  $M = 1/4$  for four different interaction strengths,  $\sigma = 0, 0.4, 0.7,$  and  $1.0$  (top to bottom). The cyan line demarks the maximal propagation speed,  $v_{\max}(M = 1/4) \approx 1.56$ .

and continuum data occurs for intermediate time steps in Figs. 21 and 23. Since we have slaved  $M\Delta = \text{const.}$ , both  $t_\zeta$  due to the UV regularization of the initial state and  $t_3$  due to cubic curvature in the post-quench Hamiltonian [Eq. (3.53)] scale as  $\Delta^3$ , implying that the effects of both types of lattice regularization can be simultaneously decreased by increasing  $\Delta$  and the system size  $L$  for fixed  $L/\Delta$ .

We do not observe the amplification of the initial inhomogeneity predicted for the pure sine-Gordon case<sup>43</sup> in the XXZ quenches. The relativistically propagating wavepacket produced by the interacting quench shows only increasing diminishment of its amplitude, for all parameter sets considered. This is consistent with the analysis of the regularized sine-Gordon theory in Sec. III D 2: at  $t = t_\zeta$ , the prefactor of the second term in Eq. (3.48) is proportional to  $(\alpha/\zeta)^\sigma$ , which is less than or equal to one for the parameters utilized to model the lattice quench.

In the Introduction, we exhibited in Fig. 3 a series of three-dimensional number density evolution plots for the lattice quenches with  $M\Delta = 3/2$  and  $\Delta = 12$ , with  $\sigma \in \{0, 0.4, 0.7, 1.0\}$ . As a benchmark, Fig. 26 depicts the  $\sigma = 0, M = 0, \Delta = 6$  “Fermi gas to Fermi gas” quench. (In this case, the quench consists merely of turning off the initial Gaussian trapping potential in a free Fermi gas.) Fig. 27 is the same as Fig. 3, but for the case  $\Delta = 6$ . The weak undulations seen in the central peak of  $\delta\rho(t, x)$  for the non-interacting quenches (top panels) in Figs. 3 and 27 occur at the “Zitterbewegung” frequency  $\omega = 2Mv_F = 4M$ . These oscillations appear in the non-relativistic regime for  $M\Delta$  not too large, similar to the single particle wavepacket dynamics discussed in Sec. III A; c.f. Eq. (3.10).

## V. SUMMARY AND CONCLUSION

### A. Summary of results

In this work, we have performed a systematic study of spatiotemporal density dynamics in a 1D model of lattice fermions (equivalent to the spin 1/2 XXZ chain), following a quantum quench. The ground state of the XXZ chain in the gapless XY phase, parameterized by the  $\hat{S}_i^z \hat{S}_{i+1}^z$  coupling strength  $|\gamma| < 1$ , is time-evolved by the non-interacting, band insulator Hamiltonian obtained by setting  $\gamma = 0$ , whilst simultaneously turning on a sublattice staggered magnetic field (chemical potential). As a probe of the quench dynamics, we introduced an additional localized inhomogeneity into the spin (fermion) density of the initial state, and computed the subsequent evolution of the density profile expectation value  $\rho(t, x_j)$  under the post-quench dynamics generated by a translationally-invariant Hamiltonian.

All quenches studied in this work feature the special property that the dynamics are generated by a simple, non-interacting band insulator Hamiltonian, characterized by a bandgap  $4M$ . By contrast, the pre-quench

initial condition is the ground state of a system of interacting fermions possessing a low energy Luttinger liquid description, except for the special case of a free Fermi gas with  $\gamma = 0$ , referred to as the “non-interacting” quench. We used the density matrix renormalization group (DMRG) to numerically compute the initial state correlation function required to determine the quench evolution in the interacting case, studying chains of 202 sites with periodic boundary conditions.

We identified a qualitative difference in the density dynamics generated by the initial state inhomogeneity for the non-interacting versus interacting ( $\gamma \neq 0$ ) quenches. For an initial state seeded with a Gaussian density bump of width  $\Delta$ , in the “non-relativistic” transport regime ( $M\Delta > 1$ ) we found only dispersive broadening for the non-interacting quench. By contrast, an interacting quench with the same value of  $M\Delta$  generates coherently propagating left- and right-moving density waves, which travel “ultrarelativistically” at the maximum band velocity  $v_{\max}(M)$  of the post-quench spectrum.

We showed that the lattice quench data obtained here could be well-captured by a regularized continuum sine-Gordon model. The continuum theory is an ultraviolet-modified version of the pure sine-Gordon quench previously studied in Ref. 43. In that work, an ultrarelativistically propagating density wave dubbed the “supersoliton” was identified as the leading asymptotic contribution to the exact result for  $\rho(t, x)$ , in the case of the interacting quench. The supersoliton exhibits a rigid shape and an amplitude that grows in time according to  $t^{\sigma/2}$ , where  $\sigma > 0$  ( $\sigma = 0$ ) for an initial state possessing (lacking) interfermion interactions. In the sine-Gordon quench, the supersoliton arises due to the relative quasi-particle *fractionalization* of the initial and final (pre- and post-quench) Hamiltonians, quantified by the anomalous scaling dimension  $\sigma/2$  of the post-quench fermions in the initial state. In this paper, we showed that fractionalization leads to a divergence at  $v_F$  in the local (Wigner) velocity distribution induced by the density inhomogeneity, for the interacting quench. By contrast, in the non-interacting ( $\sigma = 0$ ), non-relativistic ( $M\Delta \gg 1$ ) quench we demonstrated that Pauli-blocking limits the excitation to small velocities  $v \lesssim v_F/M\Delta$ .

In the interacting lattice quenches studied here, we did not observe amplification of the initial density profile, nor did we find the characteristic “s” shape of the supersoliton. We nevertheless established that the propagating density waves produced by an interacting lattice quench are well-described by the regularized sine-Gordon theory. For several of the lattice parameter sets studied, we demonstrated that the traveling waves of the corresponding continuum theory do exhibit the characteristic supersoliton shape at length and time scales much larger than we can access in the lattice version, owing to computational limitations. We interpret the waves produced by the interacting quench as “elementary excitations” of the non-equilibrium state; in the XXZ quench, these waves are “regularized” supersolitons. Using an appro-

priate lattice definition for  $\sigma(\gamma)$ , we exhibited the strong crossover of the post-quench dynamics as a function of the interaction strength.

## B. On field theory methods in quantum quenches

Beyond the particular dynamical phenomena uncovered in this paper, our work provides additional support to the idea that standard quantum field theory tools can be useful in studying strongly out-of-equilibrium physics in “realistic” microscopic models. This is non-trivial, because field theoretic methods are typically employed in condensed matter to capture low-energy, long-wavelength equilibrium phenomena such as that observed near a quantum critical point. In such established settings, lattice scale details in the form of irrelevant operators are often safely ignored, and field theory tools can be used to make robust, sometimes even exact predictions, as a consequence of *universality*. On the other hand, a sudden quantum quench in a global parameter of a many-particle system typically injects an extensive quantity of energy; it is not a priori clear that long-wavelength, continuum methods can provide a useful description of the resulting dynamics. Indeed, in the context of a quench, irrelevant operators encoding lattice-scale details present a serious formal difficulty: under far-from-equilibrium conditions, renormalizability of the low-energy field theory is not necessarily a barrier against their effects. The problem is that long-time dynamics can become sensitive to ultraviolet details, even if the renormalizable field theory (i.e., the model obtained by discarding all irrelevant operators) gives an ultraviolet finite prediction. The difficulty is compounded by the fact that operators irrelevant in the infrared become relevant in the ultraviolet, rendering perturbative treatments useless for long-time predictions.

In the lattice quench studied in this paper, irrelevant operators suppress the amplification effect seen in the pure sine-Gordon model, an integrable field theory in 1+1 dimensions. A systematic improvement of the pure sine-Gordon theory in order to describe a particular “parent” microscopic model would require a non-perturbative resummation of irrelevant operator effects, a difficult task. Nevertheless, we have demonstrated that a phenomenological regularization of the sine-Gordon theory (equivalent to the “resummation” of a *particular* irrelevant operator, characterizing the finite range  $\zeta$  of the nearest-neighbor density interactions on the lattice) gives good agreement with the XXZ chain dynamics, at least for the system sizes considered here.

## C. Open questions and extensions

A key question is the survivability of the ultrarelativistic density packet dynamics for longer times and larger system sizes. We identified two lifetimes  $t_\zeta$  and  $t_3$  that characterize the temporal duration, post-quench,

over which lattice effects on the dynamics in the initial and final Hamiltonians can be safely ignored. For fixed  $M\Delta > 1$  (non-relativistic quench), both  $t_{\zeta,3} \propto \Delta^3$ , which implies that the lattice effects can be systematically reduced by working with larger system sizes  $L$  and wavepacket widths  $\Delta$ , such that  $L/\Delta$  is held constant.

Finally, the effects of interparticle interactions in the dynamical evolution pose a particularly interesting question; would the presence of a non-trivial S-matrix for the massive, post-quench spectrum of quasiparticle excitations tend to encourage or retard the formation and/or decay of the “regularized” supersoliton? The answer likely hinges upon the presence or absence of integrability for the post-quench Hamiltonian. In particular, it would be interesting to study the density dynamics of an XXZ chain quench from the XY phase to the gapped, Mott-insulating Ising AFM that occurs for  $\gamma > 1$ .

The considerable flexibility afforded to tune control parameters in ultracold atom experiments, coupled with the excellent decoupling of these systems from the environment has brought quench physics in (near) integrable models within observational reach.<sup>9,80</sup> Despite the powerful methods developed to solve equilibrium properties, so far only limited analytical progress on non-equilibrium dynamics in integrable models has been made,<sup>26,30–32,80–82</sup> with the exception of systems that possess an underlying description in terms of free particles.<sup>23,24,27,29,33,35</sup> Numerical work using the time-dependent density matrix renormalization group (t-DMRG) by Manmana et. al. in Refs. 17 and 34 on XXZ chain quenches between and within the XY and Ising phases has revealed the “light-cone effect” predicted by Cardy and Calabrese<sup>28</sup>, as well as evidence for topological defect formation<sup>22,26</sup> upon quenching into the gapped Ising phase. These studies were limited to relatively small system sizes (50 sites). A variant of t-DMRG was used in Ref. 19 to investigate the decay of Néel order in XXZ quenches, while a hybrid Bethe ansatz/numerics approach was used in Ref. 37 to determine the evolution of a ferromagnetic domain wall state. Given the complexity of the pure analytical approaches, it seems likely that a numerical (or hybrid) scheme has the best chance of addressing the effects of interactions on the post-quench dynamics articulated in this paper.

We emphasize that even in equilibrium, the effects of integrability and irrelevant operators on correlation functions at non-zero temperature  $T > 0$  remain subjects of some controversy.<sup>42,65–73</sup> For massive 1D systems, Sachdev and Damle<sup>71</sup> gave well-reasoned arguments that transport at  $T > 0$  should be diffusive. This is also the naive expectation for a 1+1-D theory, in the absence of other special properties. However, Bethe ansatz results on integrable models appear to support the possibility of a non-zero Drude weight at non-zero temperature, indicative of ballistic transport.<sup>72,73</sup> One might expect that the incorporation of an integrability breaking perturbation (such as an irrelevant operator) introduces an additional timescale, beyond which the space-time retarded Green’s

function for the appropriate observable (e.g. a spin-spin correlation function) would transition from ballistic to diffusive behavior.

Lancaster and Mitra<sup>38</sup> have investigated a quench deep into the Mott insulating breather regime of the sine-Gordon model,<sup>2,49</sup> starting from a LL with an inhomogeneous “domain wall” density profile. In this case, the post-quench spectrum can be approximated by massive free bosons; because there is no fractionalization, the supersoliton does not occur. Quenches of an inhomogeneous LL with a domain wall density profile into the breather regime of sine-Gordon, incorporating interactions, were further investigated in Ref. 39, using the semiclassical truncated Wigner approximation (TWA).<sup>83</sup> In this case, the authors uncovered a persistent current, which could signal the preservation of ballistic post-quench transport. Previous work<sup>83</sup> has shown that the TWA provides a good approximation for quenches into the breather-dominated regime studied in Ref. 39.

With respect to the phenomena discussed in the present paper, the TWA is known to fail<sup>83</sup> in the “quantum” (breatherless) regime of the sine-Gordon model,<sup>2,49</sup> where fermionic solitons and antisolitons compose the spectrum. The supersoliton has been found at the special Luther-Emery point separating the semiclassical and quantum regimes, where there are no breathers and the fermions do not interact.<sup>43</sup> In the Ising phase of the XXZ chain, there are also no breathers, and the spectrum consists solely of interacting, fermionic spinons. Moreover, the post-quench dynamics of massive, interacting fermions may differ between the continuum sine-Gordon and lattice XXZ models.

## ACKNOWLEDGMENTS

DMRG calculations were performed with a modified version of the ALPS library.<sup>84</sup> T.C.B. and D.R.R. would like to thank Garnet Chan, Emanuel Gull, and Steven White for helpful discussions regarding the numerics. M.S.F. thanks Natan Andrei and Deepak Iyer for helpful discussions on integrable models. T.C.B. was supported in part by a DOE Office of Science Graduate Fellowship. M.S.F. and E.A.Y. acknowledge support by the National Science Foundation under Grant No. DMR-0547769, and by the David and Lucile Packard Foundation. D.R.R. was supported by the National Science Foundation under Grant No. CHE-0719089.

## Appendix A: Asymptotic analysis

In this appendix, we sketch the method used to obtain the long-time asymptotic results of Eqs. (3.23), (3.48), and (3.52) in the text. All three derive from the exact expression for the “regularized” sine-Gordon quench, Eq. (3.47).

All component integrals in Eq. (3.47) feature oscillatory Bessel function kernels; these enter through the Green's functions  $\bar{G}^{(1,2,3)}(t, y)$ , Eq. (3.9). Defining  $\gamma \equiv Mt'$ , Eq. (3.47) can be expressed as

$$\rho(t, x) = \frac{\rho_0(x - t')}{2} - \frac{c_N \alpha^\sigma \gamma}{2t'^{\sigma+1}} [I_1(t', x) + I_2(t', x)] + \{x \rightarrow -x\}. \quad (\text{A1})$$

For simplicity, we consider here only the linear response to the initial inhomogeneity  $\rho_0(x)$ , for the unregularized case with  $\zeta = 0$ . Then the integrals  $I_{1,2}$  are

$$I_1 = \int_{-1}^1 \frac{\sqrt{\frac{1+z}{1-z}} J_1(\gamma \sqrt{1-z^2}) dz}{(1-z)^{1+\sigma}} \int_{x-t'}^{x-zt'} dy \rho_0(y), \quad (\text{A2})$$

$$I_2 = \frac{\gamma}{2} \int_{-1}^1 dZ \int_0^{2(1-|Z|)} \frac{dz_d}{z_d^{1+\sigma}} \int_{x-t'Z+t'\frac{z_d}{2}}^{x-t'Z-t'\frac{z_d}{2}} dy \rho_0(y) \times \left[ \begin{aligned} & \sqrt{\frac{(1+Z)^2 - z_d^2/4}{(1-Z)^2 - z_d^2/4}} \\ & \times J_1 \left[ \gamma \sqrt{1 - (Z + \frac{z_d}{2})^2} \right] J_1 \left[ \gamma \sqrt{1 - (Z - \frac{z_d}{2})^2} \right] \\ & + J_0 \left[ \gamma \sqrt{1 - (Z + \frac{z_d}{2})^2} \right] J_0 \left[ \gamma \sqrt{1 - (Z - \frac{z_d}{2})^2} \right] \end{aligned} \right]. \quad (\text{A3})$$

The basic method is to slice up the domain of each integral into pieces belonging to one of two varieties: type (i) regions throughout which one can employ the large argument asymptotic series for the Bessel functions, and type (ii) crossover domains where one cannot. For type (i) regions, the Bessel functions are replaced by cosines; in the absence of a point of stationary phase or some other obstruction, these integrals can be systematically evaluated by repeated integration-by-parts. Successive integrations bring inverse powers of  $\gamma = Mt'$  from the cosine argument, which tend to suppress the contribution of the remainder in the long time limit. To ensure the convergence of the series obtained for a type (i) region, it is necessary to carefully consider the specification of its boundary.

Type (ii) regions, as well as points of stationary phase appearing in type (i) domains must be isolated and evaluated by expanding the rest of the integrand in the local neighborhood. A useful trick to extract the long-time, leading asymptotic contributions is to let each region boundary vary with  $\gamma$  according to a power law. For example, the dominant contribution to  $I_1$  in Eq. (A2) in the limit  $\gamma \rightarrow \infty$  comes from the narrow type (ii) region  $1 - \delta z_0 \leq z \leq 1$ , where  $0 < \delta z_0 \ll 1$ . We let  $\delta z_0 \equiv \gamma^{-\psi}$ , with  $\psi > 0$ . Then we perform iterated integration-by-parts upon the neighboring type (i) region with  $-1 + \delta z'_0 \leq z < 1 - \gamma^{-\psi}$  (assuming  $\delta z'_0 > 0$ ). To ensure that this series converges and produces a subleading contribution, one leverages an additional constraint (an upper bound) upon the exponent  $\psi$ ; for Eq. (A2),  $0 < \psi < 2$  does the job. Knowing the allowed range

of  $\psi$  in turn determines the character of the type (ii)  $1 - \gamma^{-\psi} \leq z \leq 1$  integration. In this way, we isolate and evaluate the leading contributions to  $I_{1,2}$  in the long time limit, obtaining the asymptotic behavior of Eq. (A1).

Execution of the above-described program is straightforward, but tedious; details are omitted here. In the remainder of this appendix, we indicate the results by identifying the key elements leading to the unregularized supersoliton formula, Eq. (3.23).

As discussed above,  $I_1$  is dominated by the contribution near  $z = 1$ . Expansion of the rest of the integrand gives

$$I_1 \sim t' \gamma^{2\sigma-1} \rho_0(x - t') 2^{1+\sigma} \int_0^{2\gamma} \frac{dy J_1(y)}{y^{2\sigma}} \sim t' \gamma^{2\sigma-1} \rho_0(x - t') \frac{2^{1-\sigma} \Gamma(1-\sigma)}{\Gamma(1+\sigma)}. \quad (\text{A4})$$

The  $I_2$  integration is dominated by the region with  $1 - \delta Z_0 \leq Z \leq 1$ , where  $0 < \delta Z_0 \ll 1$ . For the initial density profile, we assume the Gaussian bump in Eqs. (3.35) and (3.22). Making the change of variables  $Z \equiv 1 - u/2\gamma^2$  and  $z_d \equiv ur/\gamma^2$ , one finds

$$I_2 \sim -t' \gamma^{2\sigma-1} \rho_0(x - t') [\bar{I}_{2,a} + \bar{I}_{2,b}], \quad (\text{A5})$$

where

$$\bar{I}_{2,a} = \int_0^{2\gamma^2} \frac{du}{u^\sigma} \mathcal{K}(u), \quad (\text{A6a})$$

$$\bar{I}_{2,b} = \int_0^{2\gamma^2} \frac{du}{u^\sigma} \mathcal{K}(u) \times \left\{ \exp \left[ -\frac{(x-t')u}{M\Delta^2 \gamma} - \frac{1}{(2M\Delta)^2} \frac{u^2}{\gamma^2} \right] - 1 \right\}, \quad (\text{A6b})$$

with

$$\mathcal{K}(u) = \int_0^1 \frac{dr}{r^\sigma} \frac{1}{\sqrt{1-r^2}} J_1 \left[ \sqrt{u(1-r)} \right] J_1 \left[ \sqrt{u(1+r)} \right]. \quad (\text{A7})$$

To leading order,

$$\bar{I}_{2,a} \sim 2^{1-\sigma} \frac{\Gamma(1-\sigma)}{\Gamma(1+\sigma)}. \quad (\text{A8})$$

The dominant contribution to the kernel  $\mathcal{K}(u)$  relevant to the evaluation of  $\bar{I}_{2,b}$  obtains from the large- $u$  behavior of the non-oscillatory term

$$\begin{aligned} \mathcal{K}(u) & \sim \frac{1}{\pi \sqrt{u}} \int_0^1 \frac{dr \cos \left[ \sqrt{u} (\sqrt{1+r} - \sqrt{1-r}) \right]}{r^\sigma (1-r^2)^{3/4}} \\ & \sim \frac{u^{\frac{\sigma-2}{2}}}{\pi} \int_0^\infty \frac{dx}{x^\sigma} \cos(x) \\ & \sim \frac{u^{\frac{\sigma-2}{2}}}{\pi} \Gamma(1-\sigma) \sin \left( \frac{\pi\sigma}{2} \right). \end{aligned} \quad (\text{A9})$$

Assuming the Gaussian bump in Eqs. (3.35) and (3.22), Eq. (A6b) then evaluates to

$$\begin{aligned} \bar{I}_{2,b} &\sim \gamma^{-\sigma/2} \frac{2\Gamma(-\sigma)}{\Gamma(\frac{\sigma}{2}) (\sqrt{2}M\Delta)^{\sigma/2}} \exp[(x-t')^2/2\Delta^2] \\ &\quad \times D_{\sigma/2} \left[ \sqrt{2} \left( \frac{x-t'}{\Delta} \right) \right]. \end{aligned} \quad (\text{A10})$$

In this equation,  $D_\nu(z)$  denotes the parabolic cylinder function. Combining Eqs. (A5), (A8), and (A10) yields

$$I_1 + I_2 \sim -\frac{2Q \left( \frac{M^2 t'^3}{\sqrt{2}\Delta} \right)^{\sigma/2} \Gamma(-\sigma)}{M\sqrt{\pi}\Delta\Gamma(\frac{\sigma}{2})} F_\sigma \left( \frac{x-t'}{\Delta} \right), \quad (\text{A11})$$

where  $F_\sigma(z)$  was defined by Eq. (3.24). We obtain Eq. (3.23) from Eqs. (A1) and (A11), using Ref. 56.

### Appendix B: Fractionalization in the sine-Gordon model

In this appendix, we demonstrate that the natural quasiparticle degrees of freedom in the continuum Luttinger liquid Hamiltonian defined by Eqs. (3.15) and (3.16) are *fractionalized* with respect to the  $\psi$  fermions that appear in the continuum insulator Hamiltonian  $\bar{H}^{(f)}$ , Eqs. (3.1) and (3.19).

We begin by defining canonically rescaled boson variables

$$\Phi \equiv \sqrt{K}\phi, \quad \Theta \equiv \theta/\sqrt{K}, \quad (\text{B1})$$

so that Eq. (3.16) can be written as

$$\begin{aligned} \bar{H}^{(i)} &= \int dx \left[ \frac{u}{2} \left( \frac{d\Phi}{dx} \right)^2 + \frac{u}{2} \left( \frac{d\Theta}{dx} \right)^2 - \frac{\sqrt{K}\mu^{(0)}(x)}{\sqrt{\pi}} \frac{d\Theta}{dx} \right] \\ &= \int dx \left[ -u\chi^\dagger \left( i\hat{\Sigma}^3 \frac{d}{dx} \right) \chi - \sqrt{K}\mu^{(0)}(x) : \chi^\dagger \chi : \right]. \end{aligned} \quad (\text{B2})$$

On the second line of this equation, we have refermionized to obtain an expression in terms of some new, effectively non-interacting Dirac spinor  $\chi$ .<sup>1</sup> The field  $\chi$  carries scaling dimension 1/2 in the Luttinger liquid with Luttinger parameter  $K$ , and creates or annihilates the “natural” propagating quasiparticle degrees of freedom in that phase. The  $\chi$  particles propagate at the sound velocity  $u$ , rather than the bare Fermi velocity  $v_F$ .

Comparing Eqs. (3.15) and (B2), we see that the chemical potential  $\mu^{(0)}(x)$  has been rescaled by a factor of  $\sqrt{K}$  in the  $\chi$  language. This indicates that the  $\chi$  fermion carries a fraction  $\sqrt{K}$  of the conserved  $\psi$  fermion number charge. We can see this explicitly by considering the bosonic expressions for the components of  $\psi$  and  $\chi$ ; in terms of the original boson variables  $\phi$  and  $\theta$  in Eq. (3.16),

these read

$$\begin{aligned} \psi(x) &\equiv \begin{bmatrix} \psi_1 \\ \psi_2 \end{bmatrix} \\ &= \frac{1}{\sqrt{2\pi\alpha}} \begin{bmatrix} \exp\{i\sqrt{\pi}[\phi(x) + \theta(x)]\} \\ \exp\{i\sqrt{\pi}[\phi(x) - \theta(x)]\} \end{bmatrix}, \quad (\text{B3}) \\ \chi(x) &\equiv \begin{bmatrix} \chi_1 \\ \chi_2 \end{bmatrix} \\ &= \frac{1}{\sqrt{2\pi\alpha}} \begin{bmatrix} \exp\left\{i\sqrt{\pi} \left[ \sqrt{K}\phi(x) + \frac{1}{\sqrt{K}}\theta(x) \right] \right\} \\ \exp\left\{i\sqrt{\pi} \left[ \sqrt{K}\phi(x) - \frac{1}{\sqrt{K}}\theta(x) \right] \right\} \end{bmatrix}. \end{aligned} \quad (\text{B4})$$

Number charge conservation is associated with the  $U(1)$  transformation

$$\phi \rightarrow \phi + \frac{1}{\sqrt{\pi}}\Xi, \quad \theta \rightarrow \theta.$$

so that

$$\psi \rightarrow e^{i\Xi}\psi, \quad \chi \rightarrow e^{i\sqrt{K}\Xi}\chi.$$

Finally, we note that  $\chi$  is non-local when expressed in terms of  $\psi$  (and vice-versa) for any  $K \neq 1$ , since the right-hand side of Eq. (B4) must then involve a “string” in the argument of the exponential, i.e. an integral of the  $\psi$  current components  $\{J^0, J^1\}$  from minus infinity to the argument  $x$ ; see Eq. (3.17).

### Appendix C: Wigner functions for the post-quench quasiparticles

In this appendix, we define the Wigner functions for the particle  $a_k$  and hole  $b_k$  operators of the massive, post-quench Hamiltonian  $\bar{H}^{(f)}$  [Eq. (3.25)], in the (regularized) continuum sine-Gordon quench. We then transcribe results for the local velocity “distributions” induced by the inhomogeneous  $\rho_0(x)$  [Eq. (3.35)] for the non-interacting and interacting quenches. To simplify notation we set the Fermi velocity

$$v_F \equiv 1 \quad (\text{C1})$$

in what follows.

The particle and hole Wigner distribution functions at time  $t = 0$  (immediately post-quench) are defined by

$$n_+(k; R) \equiv \int dx_d e^{-ikx_d} \langle \bar{0} | a^\dagger \left( R - \frac{x_d}{2} \right) a \left( R + \frac{x_d}{2} \right) | \bar{0} \rangle, \quad (\text{C2a})$$

$$n_-(k; R) \equiv \int dx_d e^{-ikx_d} \langle \bar{0} | b^\dagger \left( R - \frac{x_d}{2} \right) b \left( R + \frac{x_d}{2} \right) | \bar{0} \rangle, \quad (\text{C2b})$$

where  $|\bar{0}\rangle$  denotes the ground state of  $\bar{H}^{(i)}$ , Eq. (3.15). Both the real space density profile  $\rho_{0,\pm}(R)$  (at time  $t = 0$ )

and the global distribution function  $n_{\pm}(k)$  can be extracted from Eq. (C2):

$$\begin{aligned}\rho_{0,+}(R) &= \int \frac{dk}{2\pi} n_+(k; R) \\ &= \langle 0 | a^\dagger(R) a(R) | 0 \rangle,\end{aligned}\quad (\text{C3a})$$

$$\begin{aligned}n_+(k) &= \int_{-\epsilon}^{\epsilon} \frac{dQ}{2\pi} \int dR \exp(-iQR) n_+(k; R) \\ &= \int_{-\epsilon}^{\epsilon} \frac{dQ}{2\pi} \langle 0 | a^\dagger\left(k - \frac{Q}{2}\right) a\left(k + \frac{Q}{2}\right) | 0 \rangle.\end{aligned}\quad (\text{C3b})$$

For a translationally invariant system, the ‘‘point-split’’ integration in Eq. (C3b) picks up the delta function contribution at  $Q = 0$ ; we are to take  $\epsilon \rightarrow 0$  at the end of the calculation.

From Eq. (3.27),  $a$  and  $b$  are related to the right- ( $\psi_1$ ) and left-movers ( $\psi_2$ ) via

$$a(k) = \beta(k)\psi_1(k) - i\beta(-k)\psi_2(k), \quad (\text{C4a})$$

$$b(k) = \beta(k)\psi_1^\dagger(-k) - i\beta(-k)\psi_2^\dagger(-k), \quad (\text{C4b})$$

where

$$\beta(k) \equiv \sqrt{\frac{1}{2} \left[ 1 + \frac{k}{\varepsilon(k)} \right]}, \quad (\text{C5})$$

and  $\varepsilon(k) = \sqrt{k^2 + M^2}$ .

We define  $\delta n_{\pm}(k; R)$  as the linear response to  $\rho_0(x)$ , subtracting the homogeneous (global) distribution. Using the correlation functions in Eq. (3.20) and incorporating the ultraviolet regularization  $\zeta$  as in Eqs. (3.46) and (3.47), we obtain

$$\begin{aligned}\delta n_+(k; R) &= -\delta n_-(k; R) \\ &= c_N \alpha^\sigma \int \frac{dq}{2\pi} \frac{\tilde{\rho}_0(q)}{q} e^{iqR} B(k; q) \\ &\quad \times \left[ \begin{array}{l} \text{sgn}\left(k + \frac{q}{2}\right) \mathcal{G}_\sigma\left(\left|k + \frac{q}{2}\right|; \zeta\right) \\ - \text{sgn}\left(k - \frac{q}{2}\right) \mathcal{G}_\sigma\left(\left|k - \frac{q}{2}\right|; \zeta\right) \end{array} \right],\end{aligned}\quad (\text{C6})$$

where

$$B(k; q) = \beta\left(k - \frac{q}{2}\right) \beta\left(k + \frac{q}{2}\right) + \beta\left(\frac{q}{2} - k\right) \beta\left(-\frac{q}{2} - k\right).$$

The kernel  $\mathcal{G}_\sigma(|p|; \zeta)$  is defined by Eq. (3.37). Eq. (C6) is identical to the Wigner distribution for the right-mover  $\psi_1$  in Eq. (3.36), except for the  $M$ -dependent ‘‘structure factor’’  $B(k; q)$ .

We consider first the non-interacting quench ( $\sigma = 0$ ), wherein  $\mathcal{G}_\sigma(|p|; \zeta) = \pi/2$ . We assume the Gaussian density profile  $\rho_0(x)$  in Eqs. (3.35) and (3.22). As discussed below Eq. (3.38), for the non-relativistic ( $M\Delta \gg$

1), non-interacting quench, Pauli-blocking slaves the  $k$ -dependence of  $\delta n_+(k; R)$  to that of the initial density profile  $\tilde{\rho}_0(q = 2k)$ , suppressing the contribution of momenta  $|k| \gtrsim 1/\Delta$ . Using the dispersion in Eq. (3.26) to convert momentum to velocity, we obtain the local velocity ‘‘distribution’’ at  $R = 0$  (the center of the density bump),

$$\delta n_+(v; R = 0) \sim \frac{QM}{2v^2(M\Delta)^2} \frac{\exp\left(-\frac{v^2(M\Delta)^2}{1-v^2}\right)}{\sqrt{1-v^2}}. \quad (\text{C7})$$

This equation applies when  $v \gg 1/M\Delta$ , for the non-relativistic regime ( $M\Delta \gg 1$ ) of the non-interacting quench ( $\sigma = 0$ ). The exponential strongly suppresses velocities  $v \gg 1/M\Delta$ .

For the interacting case, we are interested in a ‘‘soft quench’’ (Sec. IA 1), defined as the regime where  $1/\Delta \ll M \ll 1/\zeta$ , i.e. a non-relativistic initial condition, and an effective Compton wavelength much larger than the ultraviolet scale  $\zeta$ , which is of order the lattice spacing. As in Eq. (3.39) the position and momentum dependencies factorize. Converting to velocity, we obtain

$$\begin{aligned}\frac{\delta n_+(v; R)}{\rho_0(R)} &\sim \frac{c_1(\sigma) v^{\sigma-1}}{(1-v^2)^{1+\sigma/2}} \\ &\quad \times \left[ 1 + 2^{\sigma-1} \left( \frac{vM\zeta}{\sqrt{1-v^2}} \right)^{1-\sigma} \frac{\Gamma\left(\frac{\sigma-1}{2}\right)}{\Gamma\left(\frac{1-\sigma}{2}\right)} \right],\end{aligned}\quad (\text{C8a})$$

valid for  $(1/M\Delta) \ll v \lesssim 1 - (M\zeta)^2/2$ , and

$$\frac{\delta n_+(v; R)}{\rho_0(R)} \sim \frac{c_2(\sigma) v^{\sigma/2-1}}{(1-v^2)^{1+\sigma/4}} \exp\left(-\frac{vM\zeta}{\sqrt{1-v^2}}\right), \quad (\text{C8b})$$

valid for  $1 - (M\zeta)^2/2 \lesssim v \leq 1$ . The prefactors in these equations are given by

$$\begin{aligned}c_1(\sigma) &= \frac{(M\alpha)^\sigma \sigma \pi \Gamma\left(\frac{1-\sigma}{2}\right)}{2^{\sigma+1} \Gamma\left(\frac{1+\sigma}{2}\right)}, \\ c_2(\sigma) &= \left(\frac{M\alpha^2}{\zeta}\right)^{\sigma/2} \frac{\sigma \pi^{3/2}}{2^{1+\sigma/2} \Gamma\left(\frac{1+\sigma}{2}\right)}.\end{aligned}$$

Eqs. (C8a) and (C8b) apply to the interacting quench with  $0 < \sigma < 1$ . For  $M\zeta \ll 1$ , i.e. a Compton wavelength much larger than the lattice spacing, Eq. (C8a) exhibits a strong non-integrable singularity approaching  $v = 1$ . For any  $\zeta > 0$ , this divergence is ultimately cut off, as in Eq. (C8b). The exponential velocity suppression in the latter equation is weaker than that in Eq. (C7), and originates in the ultraviolet behavior of the regularized Luttinger liquid correlation function, rather than the initial density profile.

- \* psiborff@rci.rutgers.edu  
† tcb2112@columbia.edu
- <sup>1</sup> For a review, see e.g. T. Giamarchi, *Quantum Physics in One Dimension* (Oxford University Press, Oxford, 2004).
  - <sup>2</sup> For a review, see e.g. A. O. Gogolin, A. A. Nersesyan, and A. M. Tsvelik, *Bosonization and Strongly Correlated Systems* (Cambridge University Press, Cambridge, 1998).
  - <sup>3</sup> M. A. Cazalilla, J. Phys. B **37**, S1 (2004).
  - <sup>4</sup> For a review, see M. P. A. Fisher and L. I. Glazman, in *Mesoscopic Electron Transport*, edited by Sohn, Kouwenhoven, and Schön (Kluwer, The Netherlands, 1997).
  - <sup>5</sup> For a review, see e.g. R. Shankar, Acta Phys. Pol. **26**, 1835 (1995).
  - <sup>6</sup> D. L. Maslov and M. Stone, Phys. Rev. B **52**, 5539(R) (1995); I. Safi and H. J. Schulz, *ibid.* **52**, 17040(R) (1995); V. V. Ponomarenko, *ibid.* **52**, 8666(R) (1995).
  - <sup>7</sup> I. Bloch, J. Dalibard, and W. Zwerger, Rev. Mod. Phys. **80**, 885 (2008).
  - <sup>8</sup> M. Greiner, O. Mandel, T. W. Hänsch, and I. Bloch, Nature **419**, 51 (2002).
  - <sup>9</sup> T. Kinoshita, T. Wenger, and D. S. Weiss, Nature **440**, 900 (2006).
  - <sup>10</sup> L. E. Sadler, J. M. Higbie, S. R. Leslie, M. Vengalatorre, and D. M. Stamper-Kurn, Nature **443**, 312 (2006).
  - <sup>11</sup> C. N. Weiler, T. W. Neely, D. R. Scherer, A. S. Bradley, M. J. Davis, and B. P. Anderson, Nature **455**, 948 (2008).
  - <sup>12</sup> H. Ott, E. de Mirandes, F. Ferlaino, G. Roati, G. Modugno, and M. Inguscio, Phys. Rev. Lett. **92**, 160601 (2004); L. Pezzè, L. Pitaevskii, A. Smerzi, S. Stringari, G. Modugno, E. de Mirandes, F. Ferlaino, H. Ott, G. Roati, M. Inguscio, *ibid.* **93**, 120401 (2004); N. Strohmaier, Y. Takasu, K. Günter, R. Jördens, M. Köhl, H. Moritz, and T. Esslinger, *ibid.* **99**, 220601 (2007).
  - <sup>13</sup> U. Schneider, L. Hackermüller, J. P. Ronzheimer, S. Will, S. Braun, T. Best, I. Bloch, E. Demler, S. Mandt, D. Rasch, A. Rosch, arXiv:1005.3545
  - <sup>14</sup> A. Sommer, M. Ku, G. Roati, and M. W. Zwierlein, arXiv:1101.0780.
  - <sup>15</sup> M. Rigol, V. Dunjko, V. Yurovsky, and M. Olshanii, Phys. Rev. Lett. **98**, 050405 (2007); M. Rigol, V. Dunjko, and M. Olshanii, Nature (London) **452**, 854 (2008).
  - <sup>16</sup> C. Kollath, A. M. Läuchli, and E. Altman, Phys. Rev. Lett. **98**, 180601 (2007).
  - <sup>17</sup> S. R. Manmana, S. Wessel, R. M. Noack, and A. Muramatsu, Phys. Rev. Lett. **98**, 210405 (2007).
  - <sup>18</sup> M. Moeckel and S. Kehrein, Phys. Rev. Lett. **100**, 175702 (2008); Ann. Phys. (N.Y.) **324**, 2146 (2009); M. Eckstein, M. Kollar, and P. Werner, Phys. Rev. Lett. **103**, 056403 (2009).
  - <sup>19</sup> P. Barmettler, M. Punk, V. Gritsev, E. Demler, and E. Altman, Phys. Rev. Lett. **102**, 130603 (2009); New J. Phys. **12**, 055017 (2010).
  - <sup>20</sup> M. Rigol, Phys. Rev. Lett. **103**, 100403 (2009).
  - <sup>21</sup> J. Sabio and S. Kehrein, New J. Phys. **12**, 055008 (2010).
  - <sup>22</sup> T. W. B. Kibble, J. Phys. A **9**, 1387 (1976); W. H. Zurek Nature (London) **317**, 505 (1985).
  - <sup>23</sup> W. H. Zurek, U. Dorner, and P. Zoller, Phys. Rev. Lett. **95**, 105701 (2005); A. Polkovnikov, Phys. Rev. B **72**, 161201(R) (2005); S. Deng, G. Ortiz, and L. Viola, *ibid.* **80**, 241109(R) (2009).
  - <sup>24</sup> L. Cincio, J. Dziarmaga, M. M. Rams, and W. H. Zurek, Phys. Rev. A **75**, 052321 (2007).
  - <sup>25</sup> A. Polkovnikov and V. Gritsev, Nature Physics **4**, 477 (2008).
  - <sup>26</sup> C. De Grandi, V. Gritsev, and A. Polkovnikov, Phys. Rev. B **81**, 012303 (2010); **81**, 224301 (2010).
  - <sup>27</sup> E. Barouch, B. McCoy, and M. Dresden, Phys. Rev. A **2**, 1075 (1970).
  - <sup>28</sup> P. Calabrese and J. Cardy, Phys. Rev. Lett. **96**, 136801 (2006); J. Stat. Mech. P06008 (2007).
  - <sup>29</sup> M. A. Cazalilla, Phys. Rev. Lett. **97**, 156403 (2006); A. Iucci and M. A. Cazalilla, Phys. Rev. A **80**, 063619 (2009); New J. Phys. **12**, 055019 (2010).
  - <sup>30</sup> V. Gritsev, A. Polkovnikov, and E. Demler, Phys. Rev. B **75**, 174511 (2007).
  - <sup>31</sup> V. Gritsev, E. Demler, M. Lukin, and A. Polkovnikov, Phys. Rev. Lett. **99**, 200404 (2007).
  - <sup>32</sup> M. B. Hastings, L. S. Levitov, arXiv:0806.4283.
  - <sup>33</sup> G. S. Uhrig, Phys. Rev. A **80**, 061602(R) (2009); B. Dóra, M. Haque, and G. Zaránd, arXiv:1011.6655.
  - <sup>34</sup> S. R. Manmana, S. Wessel, R. M. Noack, and A. Muramatsu, Phys. Rev. B **79**, 155104 (2009).
  - <sup>35</sup> D. Rossini, A. Silva, G. Mussardo, G. Santoro, Phys. Rev. Lett. **102**, 127204 (2009); D. Rossini, S. Suzuki, G. Mussardo, G. E. Santoro, A. Silva, Phys. Rev. B **82**, 144302 (2010).
  - <sup>36</sup> L. Mathey and A. Polkovnikov, Phys. Rev. A **81**, 033605 (2010).
  - <sup>37</sup> J. Mossel and J.-S. Caux, New J. Phys. **12**, 055028 (2010).
  - <sup>38</sup> J. Lancaster and A. Mitra, Phys. Rev. E **81**, 061134 (2010).
  - <sup>39</sup> J. Lancaster, E. Gull, and A. Mitra, Phys. Rev. B **82**, 235124 (2010).
  - <sup>40</sup> P. Schmitteckert, Phys. Rev. B **70**, 121302 (2004).
  - <sup>41</sup> C. Kollath, U. Schollwöck, J. von Delft, and W. Zwerger, Phys. Rev. A **71**, 053606 (2005).
  - <sup>42</sup> S. Langer, F. Heidrich-Meisner, J. Gemmer, I. P. McCulloch, and U. Schollwöck, Phys. Rev. B **79**, 214409 (2009).
  - <sup>43</sup> M. S. Foster, E. A. Yuzbashyan, and B. L. Altshuler, Phys. Rev. Lett. **105**, 135701 (2010).
  - <sup>44</sup> Z. Cai, L. Wang, X. C. Xie, U. Schollwöck, X. R. Wang, M. Di Ventura, and Y. Wang, Phys. Rev. B **83**, 155119 (2011).
  - <sup>45</sup> F. Heidrich-Meisner, S. R. Manmana, M. Rigol, A. Muramatsu, A. E. Feiguin, and E. Dagotto, Phys. Rev. A **80**, 041603(R) (2009).
  - <sup>46</sup> J. Kajala, F. Massel, and P. Törmä, arXiv:1101.6025v1.
  - <sup>47</sup> F. Heidrich-Meisner, M. Rigol, A. Muramatsu, A. E. Feiguin, and E. Dagotto, Phys. Rev. A **78**, 013620 (2008).
  - <sup>48</sup> A. Luther and V. J. Emery, Phys. Rev. Lett. **33**, 589 (1974).
  - <sup>49</sup> For a review, see e.g. R. Rajaraman, *Solitons and Instantons* (North-Holland, Amsterdam, 1982).
  - <sup>50</sup> For a review, see e.g. B. Sutherland, *Beautiful Models* (World Scientific, Singapore, 2004).
  - <sup>51</sup> We employ the standard basis for all Pauli matrices.
  - <sup>52</sup> The functions  $\phi_{\{0,+,-\}}$  in Eq. (3.10) are given by
$$\phi_0 = \frac{tx^2}{M\Delta^4\delta^2(t)},$$

$$\phi_{\pm} = \frac{t[(Mx)^2 - 1]}{M^3\Delta^4\delta^2(t)} \pm \frac{2x}{M\Delta^2\delta^2(t)}.$$
  - <sup>53</sup> We employ the following definitions of the time-reversal

$\mathcal{T}$  and parity  $\mathcal{P}$  transformations in the low energy Dirac theory outlined in Eqs. (3.1)–(3.3):

$$\begin{aligned} (\mathcal{T}) : \quad & \Psi(x) \rightarrow \hat{\sigma}^1 \Psi^*(x), \quad i \rightarrow -i, \\ (\mathcal{P}) : \quad & \Psi(x) \rightarrow \hat{\sigma}^2 \Psi(-x). \end{aligned}$$

The time-reversal transformation  $\mathcal{T}$  is antiunitary and squares to one (spinless/spin-polarized fermions). These conventions are consistent with appropriate “microscopic” definitions for the lattice model in Eq. (2.3b).

<sup>54</sup> Technically, the lattice potential  $\mu_i^{(0)}$  in Eq. (2.3a) appears in the continuum as

$$\mu_i^{(0)} \sim \mu^{(0)}(x_i) + (-1)^{x_i} \mu_s^{(0)}(x_i).$$

In this equation,  $\mu^{(0)}(x) [\mu_s^{(0)}(x)]$  gives the slowly-varying envelope for the smooth (sublattice-staggered) component of  $\mu_i^{(0)}$ . We have neglected the sublattice-staggered component in Eq. (3.15), because the initial Gaussian “bump” assumed in Eq. (2.4) gives a negligible contribution to  $\mu_s^{(0)}(x)$  for  $\Delta$  larger than a couple of lattice spacings.

<sup>55</sup> See, e.g., J. Zinn-Justin, *Quantum Field Theory and Critical Phenomena*, 4<sup>th</sup> ed. (Clarendon Press, Oxford, 2002).

<sup>56</sup> The normalization constant  $c_N$  is determined by enforcing the fermionic sum rule (canonical anticommutation relations) on the correlation function  $C_j^i$  in Eq. (3.20). The result is

$$c_N = \sqrt{\pi} \frac{\Gamma(1 + \frac{\sigma}{2})}{\Gamma(\frac{1+\sigma}{2})}.$$

<sup>57</sup> We note that Eq. (3.21) is slightly different from a corresponding expression in Ref. 43. In the language of that paper, the fermion  $\psi$  appearing in Eqs. (3.1) and (3.15) denotes the LE point quantum soliton; by applying the bosonization transformation directly to  $\bar{H}^{(i)}$  as expressed in terms of  $\psi$ , the LE point is effectively shifted from  $K = 1/4$  to  $K = 1$ .

<sup>58</sup> Vertex operators are primary fields in the free boson conformal field theory; a conventional normalization scheme sets the coefficient of the 2-point correlator in Eq. (3.20) equal to one.<sup>85</sup>

<sup>59</sup> While the exact asymptotic expression in Eq. (3.23) conserves the particle number, it is not strictly causal. The function  $F_\sigma(z)$  in Eq. (3.24) exhibits a power-law tail  $\propto |z|^{-1-\sigma/2}$  for  $z \rightarrow -\infty$ , inducing a finite (i.e., not exponentially suppressed) density disturbance at arbitrarily large  $|x|$  in Eq. (3.23) for any  $t' \gtrsim 1/M$ . This is an artifact of the asymptotic analysis, not the exact bosonization result, because neglected terms in Eq. (3.23) (which feature amplitudes that decay in time) cancel these tails, shifting the acausal contribution inside the lightcone. The causal response of the exact result can be seen from the numerical integration depicted in Fig. 6.

<sup>60</sup> Although the natural quasiparticle degrees of freedom in the interacting Luttinger liquid  $\bar{H}^{(i)}$  [Eq. (3.15) with  $\gamma \neq 0$ ] are “fractionalized” with respect to the post-quench fermion  $\psi$  [Eq. (3.1)], the latter remains an eigenoperator of the renormalization group.<sup>85</sup>

<sup>61</sup> E. M. Lifshitz and L. P. Pitaevskii, *Physical Kinetics* (Pergamon, London, 1981).

<sup>62</sup> M. C. Gutzwiller, *Chaos in Classical and Quantum Mechanics* (Springer-Verlag, New York, 1990).

<sup>63</sup> J. I. Cirac, P. Maraner, and J. K. Pachos, Phys. Rev. Lett. **105**, 190403 (2010).

<sup>64</sup> See, e.g., N. Goldenfeld, *Lectures on Phase Transitions and the Renormalization Group* (Perseus Books, Reading Mass., 1992); J. Cardy, *Scaling and Renormalization in Statistical Physics* (Cambridge University Press, Cambridge, 1996).

<sup>65</sup> S. Sachdev, T. Senthil, and R. Shankar, Phys. Rev. B **50**, 258 (1994); S. Sachdev, *ibid.* **50**, 13006 (1994).

<sup>66</sup> H. Castella, X. Zotos, and P. Prelovšek, Phys. Rev. Lett. **74**, 972 (1995); X. Zotos, F. Naef, and P. Prelovšek, Phys. Rev. B **55**, 11029 (1997).

<sup>67</sup> A. Rosch and N. Andrei, Phys. Rev. Lett. **85**, 1092 (2000); K. Saito, Phys. Rev. B **67**, 064410 (2003); S. Fujimoto and N. Kawakami, Phys. Rev. Lett. **90**, 197202 (2003).

<sup>68</sup> X. Zotos and P. Prelovšek, Phys. Rev. B **53**, 983 (1996); B. N. Narozhny, A. J. Millis, and N. Andrei, *ibid.* **58**, R2921 (1998); J. V. Alvarez and C. Gros, Phys. Rev. Lett. **88**, 077203 (2002); F. Heidrich-Meisner, A. Honecker, D. C. Cabra, and W. Brenig, Phys. Rev. B **68**, 134436 (2003).

<sup>69</sup> J. Benz, T. Fukui, A. Klümper, and C. Scheeren, J. Phys. Soc. Jpn. Suppl. **74**, 181 (2005); J. Sirker, R. G. Pereira, and I. Affleck, Phys. Rev. Lett. **103**, 216602 (2009); T. Prosen, arXiv:1103.1350.

<sup>70</sup> For a recent overview, see e.g. J. Sirker, R. G. Pereira, and I. Affleck, Phys. Rev. B **83**, 035115 (2011).

<sup>71</sup> K. Damle and S. Sachdev, Phys. Rev. B **57**, 8307 (1998); Phys. Rev. Lett. **95**, 187201 (2005).

<sup>72</sup> S. Fujimoto, J. Phys. Soc. Jpn. **68**, 2810 (1999); R. M. Konik, Phys. Rev. B **68**, 104435 (2003).

<sup>73</sup> B. L. Altshuler, R. M. Konik, A. M. Tsvelik, Nucl. Phys. B **739**, 311 (2006).

<sup>74</sup> A renormalizable quantum field theory is defined<sup>55</sup> by the condition that the coupling strengths associated with all irrelevant operators are pinned to zero. This notion becomes important when exploring theories asymptotically free in the ultraviolet, such as QCD.

<sup>75</sup> S. R. White, Phys. Rev. Lett. **69**, 2863 (1992).

<sup>76</sup> S. R. White, Phys. Rev. B **48**, 10345 (1993).

<sup>77</sup> U. Schollwöck, Rev. Mod. Phys. **77**, 259 (2005).

<sup>78</sup> P. Pippin, S. R. White, and H. G. Evertz, Phys. Rev. B **81**, 081103(R) (2010).

<sup>79</sup> The ultimate long-time behavior of the regularized sine-Gordon result in Eq. (3.47) gives the pure Gaussian translation in Eq. (3.52). For the values of  $\alpha$  and  $\zeta$  employed above, the amplitude of the Gaussian is negative, compensated by a long positive density tail neglected in Eq. (3.52).

<sup>80</sup> V. Gritsev, T. Rostunov, and E. Demler, J. Stat. Mech. P05012 (2010).

<sup>81</sup> D. Fioretto and G. Mussardo, New J. Phys. **12**, 055015 (2010).

<sup>82</sup> J. Mossel, G. Palacios, and J.-S. Caux, J. Stat. Mech. LO9001 (2010).

<sup>83</sup> For a review, see A. Polkovnikov, Ann. Phys. (N.Y.) **325**, 1790 (2010).

<sup>84</sup> A. F. Albuquerque, Journal of Magnetism and Magnetic Materials **310**, 1187 (2007).

<sup>85</sup> See, e.g., P. Di Francesco, P. Mathieu, and D. Sénéchal, *Conformal Field Theory* (Springer-Verlag, New York, 1996).